Geo-information Science and Remote Sensing

Thesis Report GIRS-2018-22

APPLICATION OF STRUCTURE FROM MOTION AND A HAND-HELD LIDAR SYSTEM TO MONITOR EROSION AT OUTCROPS

Limit of detection determination of rock surface changes

Bart Middelburg

June 18, 2018

WAGENINGEN
UNIVERSITY & RESEARCH

Application of Structure from Motion and a handheld lidar system to monitor erosion at outcrops

Limit of detection determination of rock surface changes

Bart Middelburg

Registration number 93 12 0857 0110

Supervisors:

dr. H.M. Bartholomeus (WUR)
dr. A.J.A.M. Temme (Kansas State University)

A thesis submitted in partial fulfilment of the degree of Master of Science
at Wageningen University and Research Centre,
The Netherlands.

June 18, 2018
Wageningen, The Netherlands

Thesis code number: GRS-80436
Thesis Report: GIRS-2018-22
Wageningen University and Research Centre
Laboratory of Geo-Information Science and Remote Sensing

Abstract

Structure from Motion (SfM) and light detection and ranging (lidar) are widely used techniques to collect topographic data. Both techniques are perfectly suited to use at remote and hard to reach mountainous areas. A challenging factor is to determine the outdoor precision of this topographic data. In addition, there is a lack of knowledge about the effect of the sampling strategy on the quality of the data. This study covers, (1) the effect of number of photos on the precision of a DSM; (2) the capability of SfM and a hand-held lidar scanner to create consistent point clouds of an unchanged area; (3) the cell specific limit of detection (LoD) of surface changes without the need of GPS measured GCPs. The LoD takes deviations among point clouds introduced by different camera positions, alignment in the pre- and post erosion set of digital surface models (DSMs) and rasterizing into account. Differences in rasters decrease from a range of 3 cm to 0.8 cm when the photo density was increased from 3 to 18 photos m^{-2}. The hand-held lidar system ZEB1 produced point clouds of an insufficient point density and quality to determine erosion rates. A photo density of 8 photos m^{-2} was used to create 6 unique DSMs, 90% of the differences between these 6 DSMs and mean DSM are within -3 and 3 mm, which shows that SfM is capable of generating consistent point clouds. Only surface changes larger than the LoD can reliably be detected. The mean LoD of a 2 m^2 DSM is 5 mm and increased to a mean LoD of 1.7 cm for a 120 m^2 area. This increase in LoD is mainly caused by non-linear longitudinal deformation of the point clouds along the x-axis. An afterwards correction for this deformation resulted in a mean LoD of 8.3 mm. Human induced surface changes were detected, together with regions of small false detected changes. The alignment deviation between pre- and post erosion set of DSMs is not taken into account by calculating the LoD and is likely the cause of these false positives. Future work could be done on increasing this precision of the alignment among DSM sets, determine optimal raster cell sizes and evaluate the suggested sampling strategy to prevent longitudinal deformation.

keywords: lidar, ZEB1, photogrammetry, structure from motion, point cloud analysis, erosion monitoring

Table of Contents

1 Introduction **1**

2 Problem definition and research questions **3**

3 Methodology **5**
3.1 Study area . . . 5
3.2 Overview work flow . . . 5
3.3 Background SfM and lidar . . . 6
3.3.1 Principles of SfM . . . 6
3.3.2 DSLR camera settings . . . 6
3.3.3 Principles of a handheld lidar scanner . . . 6
3.4 Data acquisition . . . 7
3.4.1 Structure from motion . . . 7
3.4.1.1 Number of photos . . . 8
3.4.1.2 Level of precision . . . 8
3.4.1.3 Change detection using Limit of Detection . . . 8
3.4.1.4 Smart phone photos . . . 8
3.4.2 Lidar . . . 9
3.4.2.1 Sampling strategy and level of precision . . . 9
3.5 Processing . . . 9
3.5.1 SfM . . . 9
3.5.2 Lidar . . . 9
3.5.3 Alignment and rasterize point clouds . . . 10
3.6 Analyze rasters . . . 11

4 Results **13**
4.1 Number of photos . . . 13
4.2 Hand-held lidar scanner ZEB1 . . . 14
4.3 Level of precision . . . 14
4.4 Change detection using Limit of Detection . . . 15
4.5 Smart phone photos . . . 18

5 Discussion **19**
5.1 Number of photos and sampling procedure . . . 19
5.2 PhotoScan . . . 19
5.3 Hand-held lidar scanner vs SfM . . . 20
5.4 Alignment of point clouds . . . 20
5.5 Limit of detection . . . 21
5.6 Volume calculation . . . 22
5.7 Smart phone . . . 23
5.8 Limitations & recommendations . . . 23

6 Conclusions **25**

Appendices **33**
A High vs medium density setting PhotoScan . . . 33
B Work flow description PhotoScan & CloudCompare . . . 33
C Effect cell size on number of empty cells . . . 36
D Errors scale bars . . . 36
E ZEB1 Point cloud . . . 38
F Change detection . . . 38

1 Introduction

Erosion is a significant environmental and agricultural problem on a global scale (Pimentel et al., 1995; De Vente et al., 2013). One of the assumed impacts of climate change is an increase in the intensity of precipitation (Pachauri et al., 2014). Studies on erosion showed that more intense precipitation will enhance the amount of erosion (Kundzewicz et al., 2007). There are several types of erosion: water erosion, wind erosion, gravitational erosion and man-made erosion (Patel, 2012). Natural erosion is driven by physical, chemical, and biological processes (Turowski and Cook, 2017). High precise rate measurements are needed to understand these processes in more detail. Erosion can happen very quickly during extreme events (e.g. Lamb and Fonstad, 2010), but is in general a slow process (e.g. Bierman and Caffee, 2001). Therefore, precise measurements are needed to detect slow erosion rates over a short time span.

Erosion rate (E) can be defined as a change in surface elevation ($\triangle h$) over time ($\triangle t$):

$$E = \frac{\triangle h}{\triangle t} \tag{1}$$

There are a number of techniques to measure erosion rates. These techniques can be divided into two classes. One class is based on dating methods focussed on the $\triangle t$ component (Geyh and Schleicher, 2012). This class is mostly used to determine erosion rates over a long time-scale. The other class focusses on the $\triangle h$ component and the known $\triangle t$ between measurements. Measuring erosion rates at short time intervals requires a high precision of $\triangle h$, whereas at long timescales the importance of the $\triangle t$ precision increases.

For the $\triangle h$ erosion assessment it is in general easy to accurately determine the $\triangle t$ component. The challenge lies in getting precise topographic data at different moments in time. Next to this, it is important to compare exactly the same areas, i.e. points with the same x and y coordinates. Example techniques of this class are erosion painting (e.g. Beer et al., 2016), benchmarking (e.g. Vanwalleghem et al., 2010) and point gauging (e.g. Turowski et al., 2013).

A relatively new method to determine the $\triangle h$ component uses differences between high-resolution topographic data. Subtracting two digital elevation models (DEM) from each other will reveal the order of magnitude and spatial distribution of surface changes. Further in this report the term Digital Surface Model (DSM) will be used instead of DEM as vegetation that covers the bare soil will not be removed. In literature the terms DEM and DSM are used interchangeably (e.g. Zhang and Montgomery, 1994; Guth, 2006; Mukherjee et al., 2013).

The development of Structure from Motion (SfM) provides the opportunity for low cost three dimensional data acquisition. As in traditional photogrammetry, the principle of SfM is based on the overlap of images acquired from multiple viewpoints. SfM determines the internal camera geometry, camera position and orientation automatically and does not need georeferenced ground control points at known three-dimensional positions which are needed for traditional photogrammetry (Westoby et al., 2012). However, a local reference system is still needed to obtain real world dimensions. In addition, the need for a high degree of overlap between images taken from different position to reconstruct the full geometry remains. This gives rise to the name: structure derived from a moving sensor (Micheletti et al., 2015b).

Another technique to create a DSM is Light Detection and Ranging (lidar). Lidar has been used since the 1980s to create topographic data (Krabill et al., 1984). A light pulse is sent and the time needed to return back to the sensor is measured. As the speed of light is known, the distance to an object can be determined. Lidar is already widely used for creating topographic data over large areas (e.g. Reutebuch et al., 2003; Hladik and Alber, 2012; Aguilar et al., 2008). Lidar requires professional equipment and user expertise to process data. Both, lidar and SfM do not require direct contact with the ground to create a DSM, hence the study area is not disturbed.

The limit of detection (LoD) can be calculated with the accuracy of the pre- and post-erosion DSM. Only changes in DSMs larger than the LoD can be reliably detected. Most studies calculating the LoD were done in a controlled environment with simulated rainfall. Balaguer-Puig et al. (2017) used the SfM technique to build a DSM of 0.5 m^2 soil box in a laboratory. The amount of soil erosion measured was compared to the actual sediment yield which they used as reference volume. The average camera-object distance was 0.5 m. A raster DSM was built with a resolution of 0.01 m. They found a LoD value of approximately 1 mm. The amount of estimated soil yield using DSM of Differences (DoDs) overestimated the measured weight by 13%. Processes like compaction were not taken into account in this study and may explain the overestimation.

Prosdocimi et al. (2017) used SfM to measure soil erosion in a vineyard using a digital reflex camera and a smart phone. In total twenty photos were taken of each plot, with an object to camera distance of 1 m inside a tarpaulin covered area, creating homogeneous light conditions. For four plots of 0.25 m^2 each, they generated a DSM with a resolution of 0.01 m. The average error along the z-axis was about 0.01 m and even lower along the y and x-axis. These results were obtained for both types of cameras.

Hänsel et al. (2016) found a LoD of 3.5 mm on a 3 m^2 agricultural plot using SfM and ground control points (GCPs) as reference points. The authors suggest to reference GCP in the sub-mm range to increase the accuracy. This study took soil compaction into account and showed that this process cannot be neglected in a rain driven erosion experiment.

Other studies used lidar to determine the amount of erosion. Eltner and Baumgart (2015) used a terrestrial laser scanner (TLS) to determine the soil erosion on agricultural fields of 1000 m^2. A much larger area compared to studies done with SfM. Surface changes larger than 1.5 cm could reliably be detected.

Bechet et al. (2015) used a TLS to identify soil processes at a very small scale in 0.5 m^2 black marl soil box during a natural rain event. The TLS-object distance used was 2 m. Using a trial and error procedure they decided to use a LoD of 1.5 mm. Swelling of soil particles was observed when the soil went from dry to wet. They concluded that a TLS is capable of detecting changes at mm scale.

Within the lidar equipment there is a differentiation in price. The TLS described in the previous paragraphs is more expensive and heavier than a hand-held lidar device. Dewez et al. (2016) showed the applicability of a lidar hand-held device called ZEB1 to map an underground quarry. The precision needed to detect soil erosion is much higher compared to mapping a quarry. However, especially in complex environments, such as forests where shadow effects occur a hand held lidar scanner could be of more value compared to a stationary TLS (Bauwens et al., 2016). This could also hold for measuring erosion in complex study areas.

In general rock outcrops have a higher roughness than agriculture fields and can therefore be seen as complex areas. Steep areas such as outcrops experience high erosion rates compared to flat areas (Montgomery and Brandon, 2002). For these reasons rock outcrops are interesting areas to determine erosion using SfM and lidar. Especially, as these light weight techniques would be perfectly suited to use at remote and hard to reach mountainous areas.

Several studies used SfM and lidar to gain more insights into geological structures. Bistacchi et al. (2015) used SfM to identify faults at a rock outcrop. Riquelme et al. (2017) used SfM and lidar to extract geometrical information of rock slopes. At a larger scale SfM has been used to identify micro faults for a better risk assessment (Saputra et al., 2018). Piras et al. (2017) used drone photos as input for SfM to create a high resolution geological map.

2 Problem definition and research questions

The capability of both techniques to generate topographic data has already been proven. Numerous studies using SfM and lidar focussed on erosion rates in soil boxes in a laboratory or at agricultural fields. These fields were all homogeneous in texture and elevation. The effect of outdoor conditions on the quality of data has not been evaluated yet. In addition most studied areas were almost horizontal. Steep areas introduce new challenges to determine surface changes such as different camera-object distances and handling of point clouds under an angle. A recent study done by Gulam et al. (2018) investigated rock wall retreat and concluded that SfM is the most suitable measurement technique to explain the effect of different lithological components on the denudation rate at a rock outcrop. However, the effect of the sampling procedure on the quality of the point cloud and spatial variations between DSMs remained unclear. Hence, the limit of detection of surface changes at rock outcrops is still unknown. This research is urgently needed to enhance the use of these promising techniques at rock outcrops in practical applications.

The objective of this study is:

Determine the uncertainty in detecting surface changes at rock outcrops using Structure from Motion (SfM) or a hand-held lidar system.

To achieve this objective, the following main research question has been formulated:

- How does SfM or a hand held lidar system perform in detecting surface changes at rock outcrops in an outdoor environment and which one of these two techniques is the best?

In order to answer the main research question the following sub-questions are identified:

- How does the sampling strategy influence the precision of a DSM built with SfM or a hand-held lidar system?
- Which level of precision can be achieved by repeatedly creating DSMs of unchanged area using the SfM or a hand-held lidar system?
- What is the limit of detection (LoD) of surface changes at rock outcrops using SfM or a hand-held lidar system?

3 Methodology

3.1 Study area

The study was performed on rock outcrops around Manhattan, located in northeastern Kansas, USA (Fig. 1). The area around Manhattan experienced long-term erosion, so that the superficial deposits are generally thin and young. Limestone and shales of Permian age are the main rock types found in this region (Miller and West, 1993). The layering is composed of mostly horizontal limestone-shale couplets. As the limestone contains high chert concentration it has a high resistance to erosion (Collins et al., 1998). Chert is a quartz mineral and in the region also known as flint, this gives rise to the name of the region around Manhattan, the Flint Hills. In general the rocks are poorly exposed, except in roadcuts.

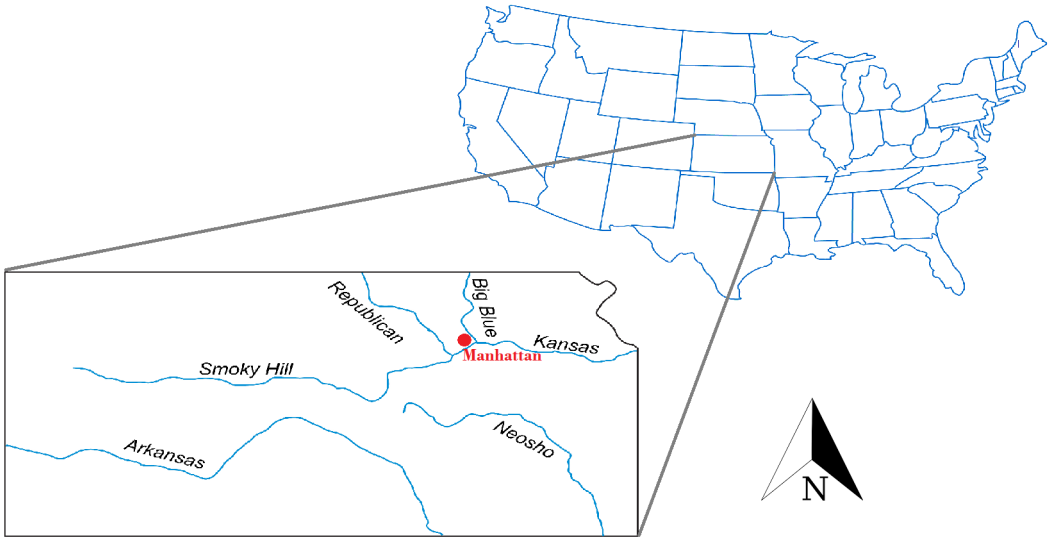

Figure 1: Map of the United States of America zoomed in on Kansas. The red dot represents the location of the city of Manhattan, where the research has been conducted.

3.2 Overview work flow

Several processing steps are needed to obtain rasters that were used to detect surface changes (Fig. 2). All steps are explained in this chapter.

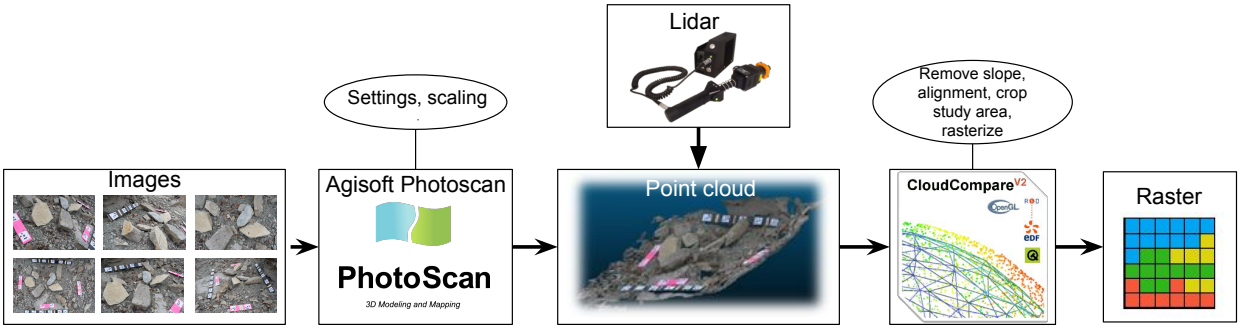

Figure 2: Work flow of using SfM or lidar to build a DSM raster.

3.3 Background SfM and lidar

3.3.1 Principles of SfM

The principle of SfM is similar to this of stereoscopic photogrammetry. A 3D model can be created using a set of overlapping photos. However, traditional photogrammetry requires known positions of the camera (Fonstad et al., 2013). SfM does not need prior knowledge of positions to reconstruct a 3D scene (Verhoeven et al., 2012). Automated image matching is a crucial step in this process.

The scale invariant feature transform (SIFT) descriptors developed by Lowe (1999) is calculated for each photo. These descriptors are robust to changes in image scale, view point and partly to light changes. They rely on multi scale image brightness and colour gradient to identify conjugate points in images. Due to the use of gradients instead of absolute pixel values an object can still be identified from multiple viewpoints. These descriptors are used to detect correspondences across the set of photos.

Correspondences between photos are refined using random sample consensus (RANSAC) (Fischler and Bolles, 1987). The transformation that maps feature points between images is estimated for every match. If a valid transformation maps a sufficient numbers of features between photos, the photos are considered geometrically verified (Schonberger and Frahm, 2016). False matches are detected using this method and only verified pairs are used in the next step.

Bundle adjustment is the last step in the SfM processing chain. Bundle adjustments refers to a process of refining the complete set of camera parameters and 3D point positions by minimizing the error of 2D observations and its 3D scene points (Triggs et al., 1999; Cao et al., 2017). A point cloud is the end product of all these steps together. The software Agisoft Photoscan automated all these steps in a user friendly way. For a detailed mathematical background of all these steps see Carrivick et al. (2016).

3.3.2 DSLR camera settings

A Nikon D5300 Digital Single Lens Reflex (DSLR) camera was used to acquire photos. This camera can take photos of 24.2 megapixels with an ISO range between 100 - 12800. The aperture controls the amount of light passing through the lens and also the depth of field.

Although used by many camera manufactures as a designation for unprocessed images, RAW is not a defined standardized format. Therefore, the photos were shot in Nikon's raw format (.NEF). In order to process them in Agisoft Photoscan there were converted to the more general raw format .DNG using the free Adobe Digital Negative Converter (Adobe Systems Software Ireland Ltd., 2018). DNG file sizes are in general 20% smaller than .NEF files and up to 90% smaller that common used .TIFF file sizes. The amount of information is equal for all extensions, only the compression is different. The quality of a point cloud depends on the settings used in the camera. In general digital photos are affected by different types of noise that have an effect on 3D modelling.

The ISO number controls the sensitivity of the sensor. A high ISO number results in a high output of the sensor for a given amount of photons compared to a low ISO. A high ISO adds more digital noise to a photo, which is visible as grains in a photo. Therefore, to capture as many detail as possible you should use a low ISO. This comes at the price that the shutter speed increases by using a low ISO.

Mapping an analogue signal into a digital range of values generates quantisation noise. The Nikon D5300 primary quantisation of RAW photos is 12 bit. This means that the minimum brightness difference that can be detected is 1/4096 of the recorded brightness range. Saving a photo as JPG uses 8 bit, which means the brightness range decreases to 255 values. Therefore, photos saved as RAW generate better outcomes than JPG. All these settings have an influence on the outcome of the estimated 3D structure. It is known that different camera settings results in different DSMs (Xiang and Cheong, 2003).

3.3.3 Principles of a handheld lidar scanner

As opposed to SfM, lidar is an active system as the device sends its own signal. The Geoslam Zeb1 hand-held mobile laser scanner (Fig. 3) combines a time-of-flight scanner with an inertial measurement unit (IMU). The scanner uses a wavelength of 905 nm and has a outdoor range of 15 m according to the manufacturer, GeoSlam Ltd.

Figure 3: Handheld lidar device: GeoSlam ZEB1 connected to the data logger.

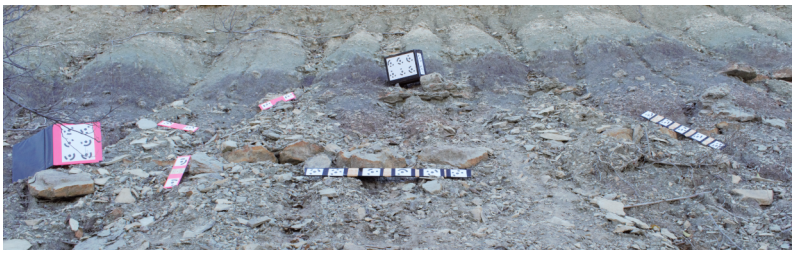

Figure 4: Overview photo of the study area analysed with different number of photos. Markers act as edges of the study area. The 6 x 100 photo sets were made at the same rock outcrop, but matched not exactly the same area.

According to Heritage and Large (2009) the distance of the sensor towards a point in space can be defined as:

$$\text{Distance} = \frac{\text{Speed of light} \times \text{Time of Flight}}{2} \tag{2}$$

The scanner does not contain a GPS system, hence the point cloud is not georeferenced. The data from both sensors is put together using a simultaneous localisation and mapping (SLAM) algorithm. The main problem which the SLAM algorithm solves is to build a consistent map of the environment while simultaneous determine the location of the device in this map (Durrant-Whyte and Bailey, 2006). In addition a correction is needed for the motion of the sensor head itself (Bosse et al., 2012). The algorithm that is used to process ZEB1 data converges to the best solution when the study contains many unique features (Ryding et al., 2015).

3.4 Data acquisition

3.4.1 Structure from motion

Photos used in this research were shot with an ISO of 800 and an aperture of f/14. A focal length of 18 mm was used for all photos. The settings of the camera were fixed as widely varying zoom settings can cause a decrease in quality in the created point cloud (Sanz-Ablanedo et al., 2012). Micheletti et al. (2015a) provide further key points that were taken into account when taking photos:

1. Plan camera survey and registration or scaling method in advance.
2. Capture the whole subject first, and then the detail, ensuring that occlusions are captured adequately.
3. Ensure appropriate coverage. Basic principle: every point on the subject must appear on at least three images acquired from spatially different locations.
4. Static scene.
5. Consistent light.
6. Avoid overexposed and underexposed images.
7. Avoid blurred images - normally arising from slow shutter speed and/or camera movement.
8. Avoid transparent, reflective or homogeneous surfaces.

The camera survey was executed in a systematic way. The procedure was to first capture the whole study area from different camera locations. Next the object to camera distance became smaller while attempting to take photos equally distributed. The other key points listed were hard to follow as sun light, wind and occurrence of reflective natural rocks cannot be controlled in the field. As these variations are part of the research, the weather and properties of the study area were described every time during the data collection.

Markers were used to give real world dimensions to the arbitrary coordinate system of the point cloud created by Agisoft Photoscan. The black circle shaped features on white paper can be generated in PhotoScan. The software can detect these unique numbered markers automatically. Markers were hand made by combining rulers with duct tape to make sure that markers remained perfectly flat. Markers were placed at bottom, right and left side of the study area. Using the markers as edges of the study area helped to capture the area of interest (Fig 4).

3.4.1.1 Number of photos

To determine the number of photos needed for a certain precision a study area of 8 m^2 was selected (Fig. 4). Sets of 25, 50, 76, 100, 150 and 200 photos were taken of this study area. It was heavily clouded, creating homogeneous light conditions during the data acquisition, which took in total 3 hours. Each set followed the procedure earlier described. It was assumed that no surface changes in the study area occurred during the data acquisition.

3.4.1.2 Level of precision

The variation within DSMs of exactly the same unchanged area was assessed by taking 6 sets of 100 photos. Each set of photos was used to build a 13 m^2 DSM. All the photos were taken within a time span of 2 hours and with equal camera settings. The area of interest was completely covered in shadow, creating homogeneous light conditions during the image acquisition. There was some wind, but there was no vegetation, resulting in a static study area.

3.4.1.3 Change detection using Limit of Detection

DSMs from different moment in times were compared to detect and quantify geomorphological changes. A DSM of differences (DoD) is obtained by subtracting two DSMs with the same origin and cell size. As the most recent DSM is subtracted from the older DSM positive values corresponds to deposition and negative values to erosion.

Subtracting two DSMs introduces the concept of error propagation. For this research there was no validation data available, hence the accuracy could not be determined. To distinguish real surface changes from noise present in the DSMs the change should be larger than the LoD (Williams, 2012). As described in Wheaton (2008) the error in a DSM was calculated from three DSMs of an unchanged surface. Each cell in a raster has a height value Z with an uncertainty δz, which can be expressed as follows according to Wheaton et al. (2010):

$$Z_{actual} = Z_{DSM} \pm \delta z \tag{3}$$

where Z_{DSM} is the mean and δz the standard deviation of the three values of the unchanged surface. This δz includes all errors caused by Agisoft Photoscan, alignment, sampling differences and interpolation methods. Brasington et al. (2003) showed that errors in DSMs propagated as follows:

$$\delta z_{DoD} = \sqrt{(2\delta z_1)^2 + (2\delta z_2)^2} \tag{4}$$

where δz_1 and δz_2 are the standard deviations of the two mean DSMs used to calculate the DoD. δz_{DoD} is the uncertainty in a DoD and is further in this thesis referred to as the limit of detection (LoD). If the value of a DoD cell is larger than δz_{DoD}, the certainty that there is a change is 95%. This method assumes that errors in each cell are random and independent. δz_{DoD} has been calculated on a cell-by-cell basis. A spatially uniform LoD will not detect small changes in areas whereas the cell uncertainty is low and detect changes in areas where the cell uncertainty is high.

A test area of 2 m^2 was used to test the concept of a cell specific LoD. In this area several stones were placed. Three sets of each 30 photos were taken. Before the next three sets of 30 photos were shot the stones were relocated to represent erosion and deposition. There was no volume added in relocating the stones, except the occurrence of air spaces underneath rocks.

Next, the size of the area was increased to a nearly vertical road cut of 120 m^2 to represent a more practical situation. In total 6 sets of 600 photos were taken, 3 sets before a self imposed erosion event and 3 sets after. The erosion event consisted of big blocks falling of the road cut and some rills of a couple of mm thick (Fig. 5). This difference in magnitude in erosion allowed testing the change detection with LoD to the fullest.

3.4.1.4 Smart phone photos

Nowadays, almost every smart phone has a built in camera. Instead of using a relatively large DSLR camera, smart phones have been used to build DSMs using SfM (e.g. Vinci et al., 2017; Wróżyński et al., 2017; Muratov et al., 2016). A smart phone has the advantage being easy to carry around and being widely available. However, the quality of photos decreases and the lens could lead to distortion (Micheletti et al., 2015a). To investigate the possible use of smart phones in erosion monitoring, 1 set of 900 photos of the large post erosion outcrop were taken in the same time as 600 photos with a DSLR. A Samsung Galaxy S7 with a focal length of 4.2 mm and a resolution of 4032 x 3024 was used. This DSM of the smart phone was compared to the mean of the 3 post erosion DSMs of the DSLR.

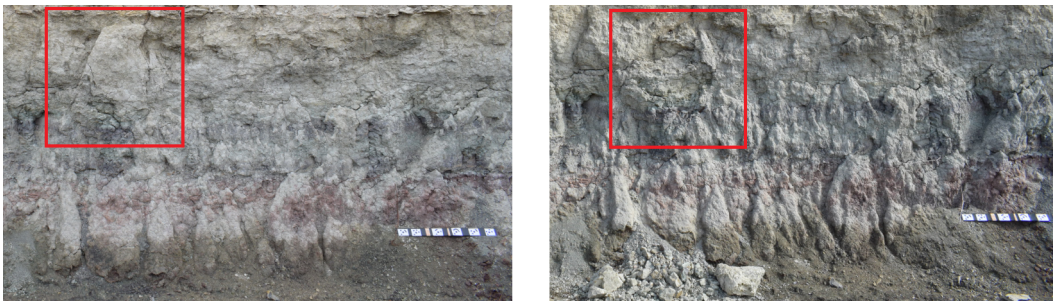

Figure 5: An example of the erosion created to observe change detection. The area in the red square has been changed. The weather conditions changed during the data acquisition, left it was cloudy whereas at the right image it was sunny.

3.4.2 Lidar

Most data acquisition key points for SfM are valid for lidar as well. However, outdoor light conditions are not important. This makes lidar less dependent on outdoor conditions than SfM. The factor rain will influence the measurements a lot, as most of the signal is absorbed or reflected in another direction at wet areas. Therefore no data has been acquired during rainy days.

Preferably the study area you are going to measure is static. However, the SLAM algorithm is capable of dealing with some moving objects who will be removed out of the point cloud (Bailey and Durrant-Whyte, 2006). Windy conditions are therefore not favourable, as vegetation will move during the data acquisition. Two features with clear edges were placed in the study area. One box of 30 x 20 x 15 cm and an A4 ring binder (Fig. 4). This to enhances the working of the algorithm and have distinguishable features in the point cloud that can be used for the alignment. A metric coordinate system is automatically generated for the point cloud as the speed of light is known.

3.4.2.1 Sampling strategy and level of precision

Scan times of 1, 2, 3, 4, 5 and 8 min were used to determine the effect of scan time on the precision of a DSM. The 8 min scan was used as to create the reference DSM. However, during this study the quality and alignment of the lidar point clouds turned out to be far from sufficient to quantify differences in DSMs caused by different scan times. An attempt of 6 scans of each 5 min resulted in data that could be processed and analysed. This already showed that the hand held lidar system was not capable detecting surface changes at a small scale. Therefore, lidar was not further analysed than the repeatability of creating DSMs of an unchanged area.

3.5 Processing

3.5.1 SfM

The computer used for the processing consisted of: Intel Xeon Processor E5 (1620 @ 3.6 GHz, single CPU), 16 GB ram, 1 tb HDD and a NVIDIA Quadro K2200 4 GB graphics card. PhotoScan offers a user friendly interface which allows users with little experience to produce point clouds from photos. However, throughout the work flow numerous parameter settings can be changed by expert users (Agisoft, 2014). The main settings used in Agisoft Photoscan are shown in Table 1. The influence of the setting building a dense point cloud at high or medium did not have significant influence (App. Fig. A.1). Morgan et al. (2017) advised to use photo alignment setting "highest" and dense point cloud quality set to "medium" to detect surface changes in laboratory flume. An elaborate sensitivity analysis for settings in PhotoScan is not part of this research and therefore this advice has been followed. For a detailed work flow description see Appendix B.

3.5.2 Lidar

The raw data acquired by the ZEB1 was saved on the connected data logger. The raw laser data must be uploaded to GeoSLAM online data processing server for conversion to a 3D point cloud using their unique sweep matching SLAM algorithm. Every conversion requires a payment of tokens. The amount of tokens depends on the length of the walking path. After the conversion the point cloud can be downloaded with a .laz extension, which directly can be used for further analysis.

Table 1: Photoscan parameter settings.

SfM parameters	Setting
Marker tolerance	60
Photo alignment	Highest
Pair preselection	Generic
Key point limit	Default: 40.000
Tie point lmit	Default: 1000
Reprojection error	0.5
Dense point cloud quality	Medium

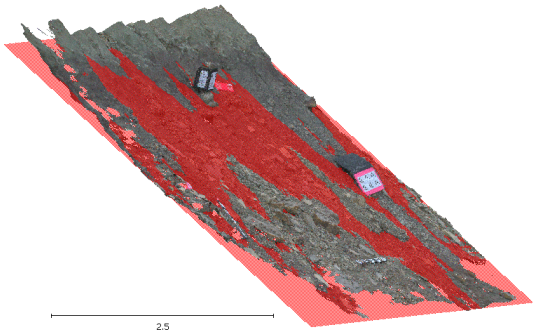

Figure 6: Fitted red plane through a point cloud that is under a certain angle. Scale bar in [m].

3.5.3 Alignment and rasterize point clouds

Point clouds produced with SfM or lidar required processing for further analysis. The study areas in this research were under a slope. When rasterizing a point cloud under a slope the average height per cell will be dominated by the height difference caused by the slope. Therefore, the point clouds were put horizontal using CloudCompare v2.6.2 (Girardeau-Montaut et al., 2018). This was achieved by fitting a plane through the point cloud under an angle (Fig. 6). The obtained transformation matrix was used to put the x and y axes along the normal direction of the plane.

To compare rasters it is important that corresponding cells are compared, i.e. the exactly same area should have the same x and y coordinates. Therefore, the point clouds should be aligned. Several algorithms align point clouds automatically (e.g. Tam et al., 2013; Rusu et al., 2008; Makadia et al., 2006). These algorithms will not work for point clouds of areas that experience a lot of surface changes as point cloud characteristics will become different. Automatic alignment would probably have worked for cases in this study. However, this has not been done to assess the added uncertainty when manual alignment is necessary.

At least 3 corresponding static points are required to align two point clouds. In this research markers used for scaling were also used as static alignment points. It is important to note that the alignment points on markers were picked manually as no function exists that automatically detects markers in CloudCompare. Two point clouds overlay when 3 corresponding alignment points were picked and aligned (Fig. 7).

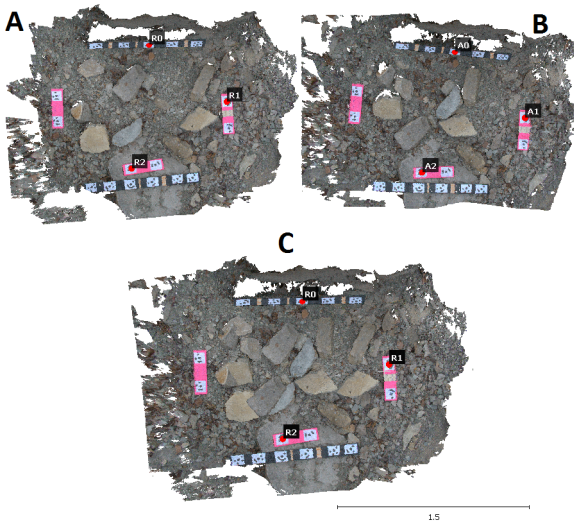

Figure 7: Alignment of two point clouds, A and B. Both show a point cloud of the same area only most of the stones have been moved. The markers are static in time and can therefore be used as alignment points represented by R0, R2 and R3 in A and A0, A1 and A2 in B. The result of the alignment is shown in C, the two point clouds overlay each other as can be seen at the merged stones. Scale bar in [m].

The cropping tool was used to cut out the area of interest in aligned point clouds. The edges of the area of interest in this research were defined by the markers. The last step in CloudCompare is to rasterize the point clouds. Cell size is the most important variable for this tool as cell size is a trade off between point support and the scale changes can be detected. A cell size of 2.5 mm was used for the whole study concluded from analysis with different cell sizes (App. Fig. C.1). Lu et al. (2017) recommended to use the finest possible grid size where no big gaps due to lack of point support occur in the raster.

3.6 Analyze rasters

Rstudio (RStudio, 2018) was used to analyse all DSM rasters. First all rasters of a set needed to be resampled to one reference raster, as the origin of rasters differed in the order of 0.1 mm. This is probably caused by the rasterize tool of CloudCompare which uses the extent of the points in the cloud. This creates a slightly different origin for rasters of the same area. The choice of the reference raster to resample is arbitrary and did not influence the results. Resampling to different resolutions introduces different outcomes when rasters are used for calculations (Dixon and Earls, 2009). As the resolution was not changed together with the origin off set of 0.1 mm minor effects of resampling are expected.

Differences between rasters were calculated with subtraction. As reference raster the DSM created with highest number of photos or the mean of a set of rasters was used. This resulted for each compared raster in a raster containing the differences. These differences have been used to create a box plot with a 5^{th}, 25^{th}, median, 75^{th} and 95^{th} percentiles.

A correction was done on a trend in differences of the large study area. The first pre erosion DSM was used as a reference to all other DSMs. Through each individual row of the raster of differences a second order polynomial model was fitted. This model was used to apply a correction to the original DSM. All DSMs were corrected to the reference DSM, the reference DSM itself was not corrected for the doming effect.

4 Results

4.1 Number of photos

DSMs created with a different number of photos resulted in similar height patterns (Fig. 8). An exception is the bottom right corner of DSM E created with 50 photos which shows low values compared to the other DSMs. The number of no data cells increases, when the number of photos per area decreases.

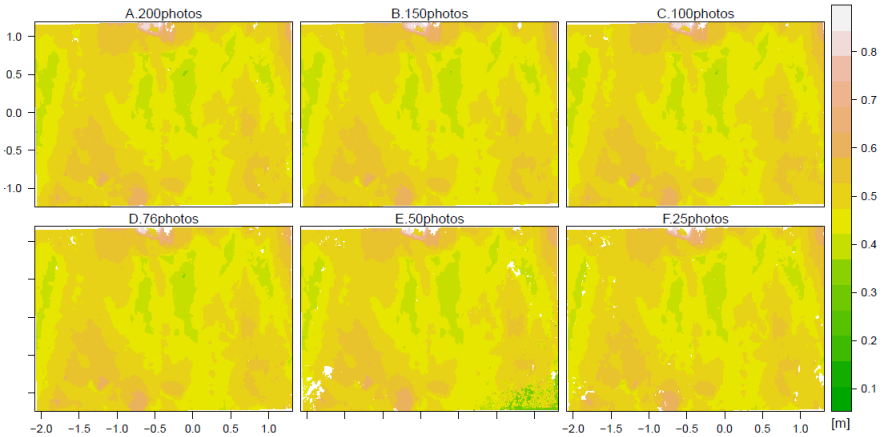

Figure 8: 6 DSMs with a cellsize of 2.5 mm each created with a different number of photos. All 6 DSMs cover exactly the same area. The lowest value of the 6 DSMs has been set as the zero reference level.

The point density depends on the number of photos (Tab. 2). The DSM created with 18 photos m^{-2} shows the highest point density, followed by the point cloud created with the highest photo density. The lowest density of photos results in the lowest point density.

A large number of photos m^{-2} decreases the range of differences between DSMs (Fig. 9). The DSM created with 200 photos was used as reference to the other DSMs. The number of photos were recalculated to a photo density to present a more generic number. The three DSMs with lowest photo density show a similar spread compared to the reference DSM, whereas from 12 photos m^{-2} on the deviations decrease. The 95^{th} percentile of the 6 photos m^{-2} DSM shows a large deviation.

Table 2: The average point density of the point clouds used to build the DSMs.

Photo density [photos m^{-2}]	Point density [pts cm^{-2}]
24	265
18	282
12	180
9	203
6	111
3	71

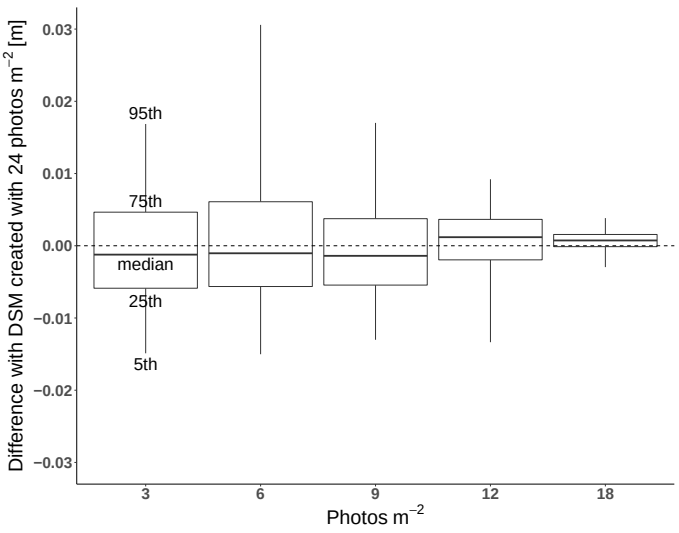

Figure 9: Boxplot of differences between DSMs with reference DSM. Horizontal line represents 0 difference line.

4.2 Hand-held lidar scanner ZEB1

All lidar based DSMs show a large number of no data cells (Fig. 10). The DSMs A, C, E and F show similar height patterns and values. DSMs B and D show height values up to 0.5 m higher. The rasters have an average point density of 7 cm^{-2}. The point clouds showed a scan range of 8 m for the ZEB1. The generated point clouds do not show clear boundaries at distinctive features. An example of a vague boundary is shown in Appendix Figure E.1, which is a traffic sign which stood near the scanned outcrop. The RMSE reached by the manual alignment of the point clouds was on average 0.21 mm, whereas with SfM RMSE in the order of cm was achieved.

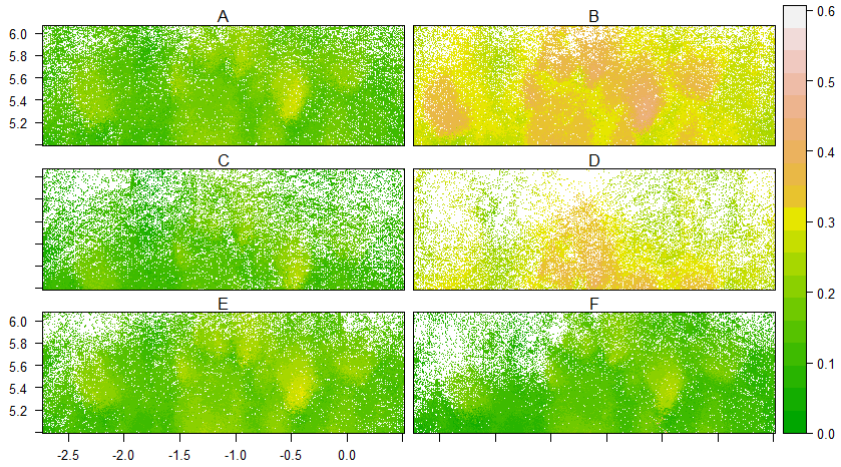

Figure 10: 6 DSMs with a cell size of 2.5 mm each created with a point cloud of a 5 min ZEB1 Scan. All 6 DSMs cover exactly the same area. The lowest value in the set of DSMs was set to zero.

4.3 Level of precision

DSMs created with a constant photo density result in visual similar surface models (Fig. 11). In between the higher elevated areas lower elevated areas are found. DSM C has some more cells with no data in the bottom right corner compared to other DSMs. At the top middle a higher situated area is located with a lot of no data cells. According to PhotoScan, the absolute error of markers is 2 mm, the reprojection error around 0.8 and effective overlap around 3.0 on average for the 6 point clouds (App. Tab. D.1).

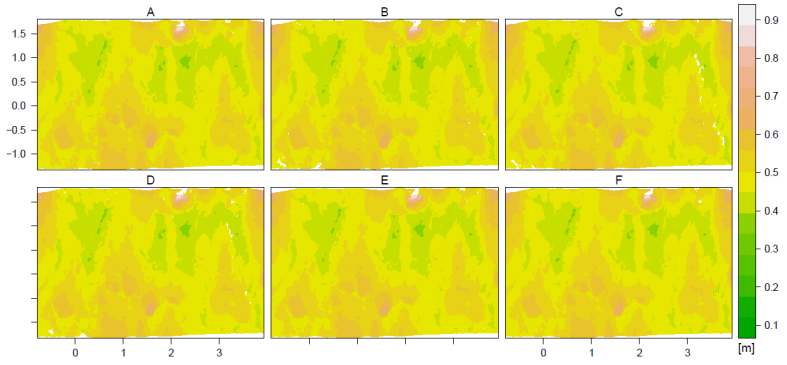

Figure 11: 6 DSMs with a cell size of 2.5 mm each created with 100 unique photos and same settings in Photoscan. All 6 DSMs cover exactly the same area. The lowest value of all DSMs has been set as the zero reference level.

The range of variation in DSMs created with equal parameters is small. All median differences with the mean DSM are within 1 mm (Fig. 12). The 25^{th} and 75^{th} percentiles are around 0.5 mm located from the median. The differences with the mean DSM are smaller than differences observed in Section 4.1 with an equal photo density.

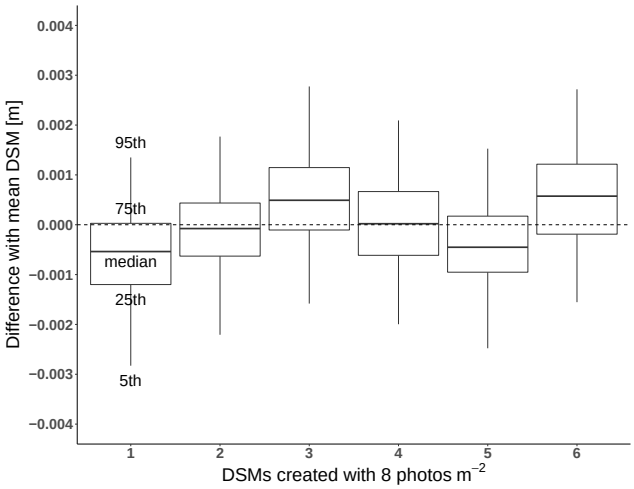

Figure 12: Box plots of the difference between DSMs created with 100 photos shown at the x-axis with the mean DSM in m. The 95th, 75th, median, 25th and 5th percentiles are shown. The horizontal dashed line represents the 0 line.

4.4 Change detection using Limit of Detection

The LoD in the small area for the procedure ranged from 4.9 10^{-5} m to 0.153 m with a mean of 5 mm. The spatial distribution shows especially high values at the edges of the rocks (App. Fig. F.1). When a pixel does not contain a value in one of the 6 DSMs no LoD or difference between the mean DSMs was calculated.

The differences between the mean DSMs overlay the relocated rocks on the background represented with the hillshade (Fig. 13). The mean DSM of the post erosion situation was subtracted from mean pre erosion situation. Only differences that are greater than the LoD for a cell are plotted. The positive values represent the former locations of the stones, whereas the negative values overlay the rocks seen in the hillshade in the background. Pixels with minor changes in the order of 1 mm are found over the whole study area. No other surface changes than the relocation of rocks were made during photo acquisition.

The total volume remained the same during the replacement of the rocks. The volume for each raster has been calculated using the cell size and height value. The difference in volume between the mean pre and post DSMs is 3.0 dm^3 on the total volume of 126.8 dm^3 of the pre erosion DSM.

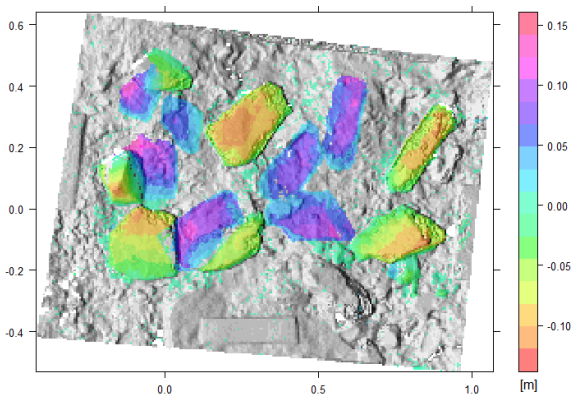

Figure 13: Map of differences between the mean pre erosion DSM and the mean of the post erosion DSM. In the background the hillshade of the mean post erosion DSM. Only differences larger that the LoD are plotted.

The LoD distribution for the large area shows a high spatial variability (Fig. 14). All the 6 DSMs (App. Fig. F.2) used to calculate the LoD were made with 600 photos each. The average LoD is 1.7 cm. At the top of the study area more cells with no data occur than at the bottom. The large area shows LoD values of 1 cm with ridges of LoD of 5 cm, except for two regions with low LoD values between -18 and -15 and between 7 and 10 on the x-axe. These regions with low LoD values can only be explained by low standard deviations between DSMs.

Differences between the mean pre and post erosion DSM along the x-axis a trend can be observed when looking in detail per row (Fig. 15a). The differences are deformed along the x-axe, further referred to as longitudinal deformation. The differences are in the range of -1.3 cm to 1 cm and have a parabolic shape opening up. The areas around -18 and 8 show differences close to 0. Most of the points should be on the zero difference line, as they did not experience any change during the data acquisition.

The differences come closer to 0 when the trend is removed every individual row (Fig. 15b) . As a result, the large study area gets a more homogeneous LoD. The new distribution of LoD has a mean of 8.3 mm. The former low LoD regions still are the most dominant low LoD regions (Fig. 16).

At the major part of the large study area no surface changes are detected (Fig. 17). The big block falling down the outcrop shown in Figure 5 is detected at location (5,0). Left of this block, several letters have been drawn of a couple of mm thick. These are not detected as surface change greater than the LoD. A smaller block was removed around location (-12,-1) and is detected. Equal observations can be done when the non-corrected LoD is used (App. Fig. F.3). At all other places where changes are detected no surface changes were made. More false changes are detected when the LoD without deformation has been used, especially at the rows where the big block was removed.

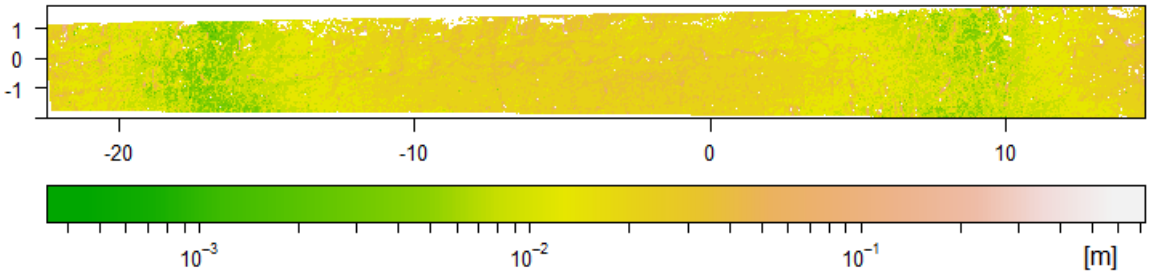

Figure 14: The Limit of Detection of the large area with longitudinal deformation. The legend has a logarithmic scale.

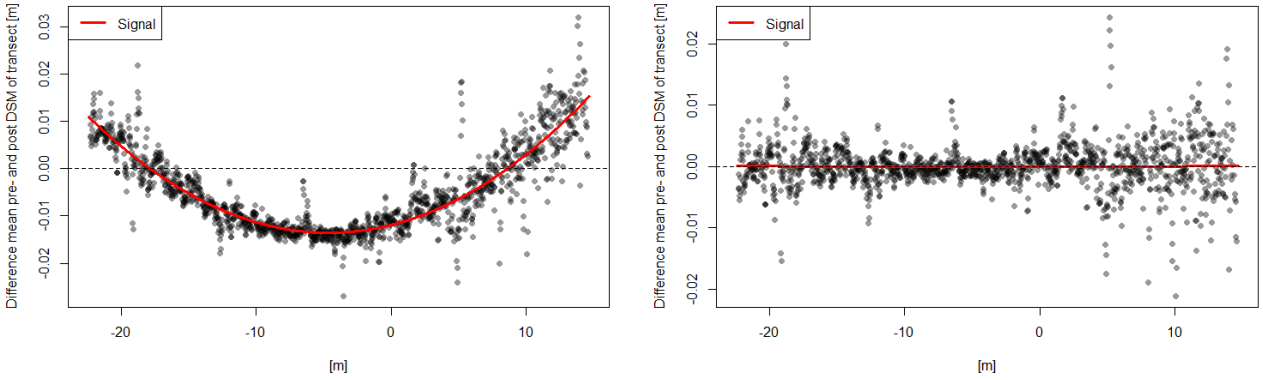

(a) Longitudinal deformation

(b) Longitudinal deformation removed

Figure 15: Differences between the mean of the pre- and post erosion DSM for the row of pixels at y value -1 m of the large area. Every point represents the mean difference over 2.5 cm along the x-axis. The red signal line is the best second order polynomial fit. Dashed line is the zero difference line. The x-axis shows the values of the arbitrary coordinate system, equal to x-axes in Figures 16 & 17.

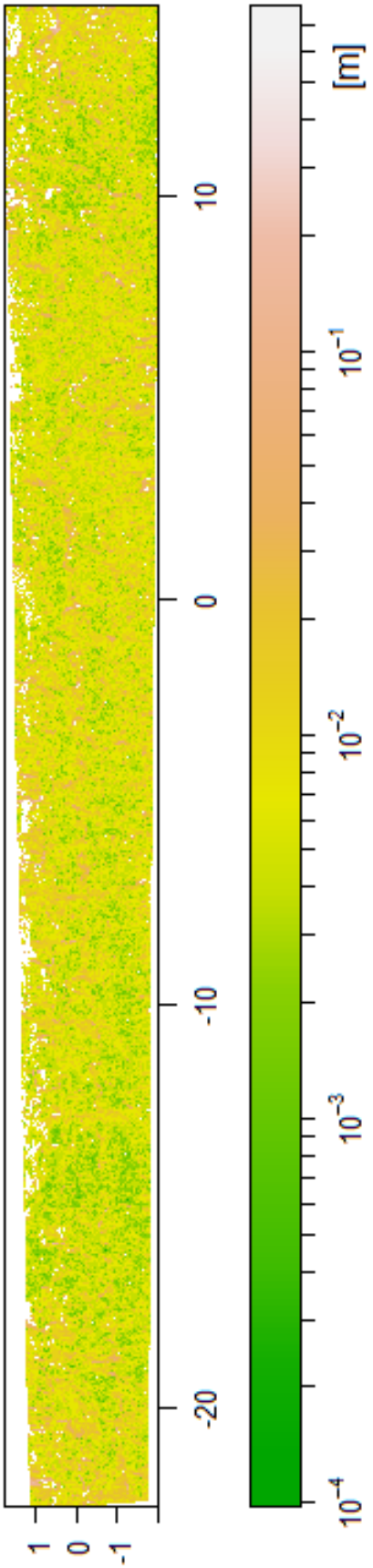

Figure 16: Limit of detection per cell of the large study area when the longitudinal deformation has been removed.

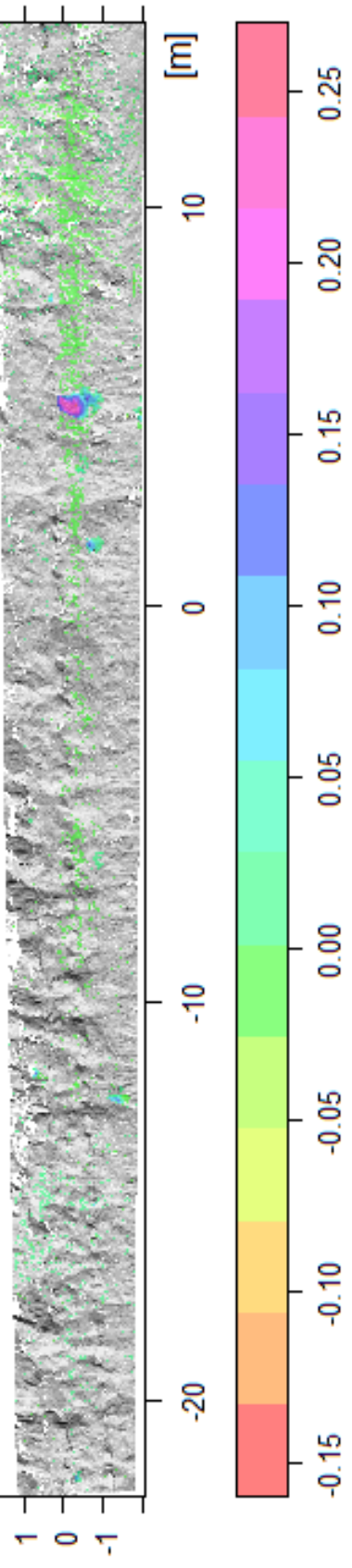

Figure 17: Difference between the mean of the 3 DSMs before erosion and mean of 3 DSMs after erosion. Only changes larger that the LoD of Fig. 16 are plotted on the hillshade of the outcrop

4.5 Smart phone photos

The DSM created with 900 smart phone photos shows large deviations from the mean DSM created with the DSLR (Fig. 18). The area left of the x-axis value -5 shows alternately positive and negative differences. The area between x values -5 and 8 shows a more homogeneous difference of 1 cm, whereas more to the right the pattern of negative and positive differences continues. Overall, the median of the differences is 7.7 mm and an absolute mean difference of 2.76 cm. Parameters in PhotoScan describing the quality of the point cloud show a large reprojection error compared to the other point clouds (App. Tab. D.2).

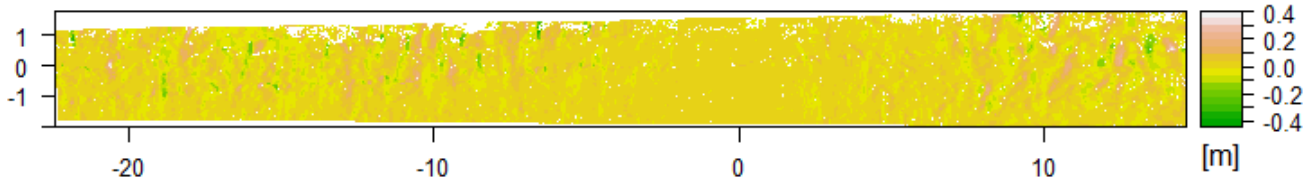

Figure 18: Map of differences between the mean of the 3 DSMs created of the post erosion situation minus the 1 DSM created with the Samsung Galaxy S7. Both DSMs were corrected for the doming effect. The absolute mean difference is 2.76 cm.

The point density for the DSM of the cell phone is lower than all other point clouds created with the DSLR (Tab. 3). The average point density is highest for point cloud number 1, whereas point cloud 3 to 6 show an equal point density around 35 points cm^{-2}. The outdoor conditions during the photo acquisition changed from cloudy to sunny during the acquisition of the 3rd set of photos.

Table 3: The average point density of the point clouds used to build the DSMs of the large areas.

Point cloud number	Point density [pts cm^{-2}]
1	68
2	44
3	36
4	37
5	34
6	36
Smartphone	20

5 Discussion

5.1 Number of photos and sampling procedure

Every survey, even with an equal number of photos will have different camera positions. The position and number of camera positions influences the quality of a point cloud. As every photo will capture an area from a different orientation or distance, the representation of especially rough surfaces in a point cloud will be different. Building a point cloud with a low number of photos, the importance of the quality per photo increases. This positioning uncertainty is one of the main reasons that no point cloud will be exactly the same. The positioning uncertainty is also seen by the use of lidar (Hodge, 2010). However, at a certain number of photos the point cloud will be only different at such a small scale that it does not affect a raster.

These effects are observed in this study as the range of difference for low photo densities compared to the high photo density reference DSM is large. Too little coverage in the right bottom corner caused false photo alignment for DSM E (Fig. 8) as the bottom right corner shows low values compared to the other 5 DSMs. There is no false alignment for the DSM created with 3 photos m^{-2}. However, it indicates from 6 photos m^{-2} and lower the alignment procedure can be negatively affected. This can be explained by the fact that complete covering of the whole area becomes difficult. In addition, there are less photos to compensate for photos with a bad orientation. Manual adjustments in the alignment could repair this, but to objectively judge differences in the work flow all the steps were kept automated. These findings are in agreement with Piermattei et al. (2015), who concluded that more images resulted in better coverage and quality of the point cloud.

Besides the false photo alignment, the raster DSMs created with 3, 6 and 9 photos m^{-2} show other differences with the reference DSM. The differences of the 12 photos m^{-2} DSM show a smaller range, despite the fact that the point density is lower compared to the 9 photos m^{-2}. The DSM created with 18 photos m^{-2} has a small range of differences and shows that only little detail is added when 24 photos m^{-2} is used. The point density supports this finding as a large increase is found towards 18 photos m^{-2}, but 24 photos m^{-2} shows a similar density. It can be concluded that there is no linear relationship between point density and the number of photos.

Creating 6 DSMs without varying the number of photos m^{-2} results in very small differences among the DSMs. All median values lie between -1 mm and 1 mm of the mean DSM. This can be partly explained as the mean of the 6 DSMs will smooth the differences slightly. Moreover, it shows that applying SfM without varying any variables produces consistent point clouds.

Micheletti et al. (2015a) found a non linear relationship between the number of images used to build a point cloud and the accuracy. There is too little data to support this finding. However, an important note for this conclusion is that increasing a low number of photos will not immediately lead to better precision of a point cloud, as the median, 25^{th} and 75^{th} percentiles do not differ a lot for 3, 6 and 9 photos m^{-2}. Using the unit photos m^{-2} does not give you direct information about the object camera distance, even though it is known that the uncertainty in a point cloud increases when the camera object distance increases (Eltner et al., 2016).

Micheletti et al. (2015a) used 13 photos of a DSLR to build a point cloud of a 12 m^2 area in PhotoModeler software. They assessed the quality using a distance tool which computes for each point the distance to the nearest point. These distances are interpreted as errors, which had median error of 0.0038 m compared to a TLS reference point cloud, using a maximum distance of 0.1 m to isolate outliers. This median is higher than medians found in this study, which can be caused by the lower photo density used. Analysing geomorphological processes using rasters it is advised to look at the error in rasters instead of cloud distances.

5.2 PhotoScan

The quality setting in PhotoScan used to create a dense clouds determines the point density. Morgan et al. (2017) showed that using the highest setting for the alignment of the photos and a medium quality for generating a point cloud produced the same median and RMS for differences between these point clouds when using only the highest settings. This is in agreement with results of this study. For surface change monitoring the medium density quality can be used, especially because using the highest setting will increase the processing time from hours to days. In addition, the size of the point cloud will increase which requires a high processing capacity computer for further analysis.

The automatic marker detection worked easy and fast. This is not in line with findings of Morgan et al. (2017). Who mention that PhotoScan was not capable of detecting markers automatically. This is even more surprising because they used a photo density an order higher than maximal used in this research. This could be explained by the use of an extremely low marker tolerance. Instead they manually picked the points, which is time consuming compared to the automatic detection. The effect of the number of markers on the quality of the point cloud has not been investigated. This could have affect the quality in the middle of the point cloud, as Gindraux et al. (2017) found that the accuracy of a DSM decreases when the distance to a GCP increases. The use of markers as the edge of the area of interest worked conveniently.

PhotoScan can generate a report which includes uncertainty parameters that are suitable for a first quality assessment. These parameters were constant for the 6 point clouds created with an equal number of photos. This matches with the small deviations found in the rasters created from these point clouds. The same holds for the parameters of the point clouds of the large study area, showing similar values among each other. Only the effective overlap was lower for the first point cloud, which suggest that accidentally more photos with a small distance to the outcrops have been taken. This could explain why PhotoScan was able to generate more points compared to the other 5 point clouds, as more detail could be reconstructed. In general PhotoScan is capable of creating dense point clouds compared to other photogrammetry software (Chidburee et al., 2016).

The higher reprojection error for the point cloud created with a smart phone indicates a lower quality point cloud. The effective image overlap is higher as 900 photos have been used compared to 600 for the other 6 point clouds. Unfortunately, this report generation function containing these parameters was found during the research and could not be applied on the point clouds created with different number of photos for the first research question. Only for the purpose of a first quality assessment these parameters are valuable, as Smith and Vericat (2015) concluded that the measured error is always higher than the theoretical error shown in the software.

5.3 Hand-held lidar scanner vs SfM

The hand-held lidar scanner is not able to produce a point cloud of sufficient quality to detect surface changes. First, the scanned areas were under a slope which made it difficult to walk at a constant pace and reach areas further up the slope. This especially became difficult when the range turned out to be 8 m instead of the 15 m described by the manufacturer. In addition the algorithm was not able to reconstruct the area without a lot of noise. This could be explained by the homogeneous surface texture of the study areas without clear features.

These results are contrary to findings of James and Quinton (2014), who found that the ZEB1 was able to scan a coastal cliff of 150 m^2 with a RMSE of 20 mm and 18 mm for SfM point to point differences compared to a reference TLS using automated alignment. They concluded that the ZEB1 should join SfM as a technique to consider when planning surveys. The use of point to point differences to asses the quality suggests a precision that never can be reached using raster differencing for the ZEB1 using small cell cizes.

Sirmacek et al. (2016) found point densities of 1000 to 18000 pts m^{-2} for the ZEB1 with one walking path through a building. These point densities were not sufficient to recognize visually fine features. The scanning time of 5 min used to create a DSM resulted in a point density of 70000 pts m^{-2}. The point density was heterogeneous in space, as there are a lot of no data cells. Even despite the higher density, features were hard to distinguish, even more as the point cloud generated with the ZEB1 is not RGB coloured as opposed to SfM point clouds.

5.4 Alignment of point clouds

The alignment of ZEB1 point cloud was difficult due to the lack of colouring. As the alignment was done by picking points manually, it was hard selecting precisely the edge a feature. This is one of the reason why the range of values in the 6 lidar DSMs is so large. In the future this problem could be partly solved by the new version of the ZEB1, the REVO1. The REVO1 can be used together with two Go Pro cameras allowing the point cloud to be coloured, which enhances the manual aligment (Nocerino et al., 2017).

The alignment with markers used for scaling in PhotoScan worked convenient. As the markers have a really small point to pick in the middle the extra deviation added with the alignment remained small. For future work the use of the marker detection in PhotoScan and automatic alignment using these markers would speed up the procedure. A key point to detect changes over time are stationary alignment points when an arbitrary coordinate system is used.

Natural features such as big rocks could be used when the monitoring time is limited and the natural alignment points do not experience significant erosion itself. Another solution could be drilling in big screws at the edges of the study area. Depending on the accessibility and legislation of the study area one of the two options could be used.

Putting steep areas horizontal is only possible when the slope of the area of interest is constant. When applying this technique to a bigger area with variation in slopes or slopes alternated with horizontal planes detecting surface changes using raster DoDs becomes impossible. A raster should always be created along the normal direction of the surface. Chen et al. (2017) describes different algorithms that are capable of compensating for slope present in a point cloud, however the quality of these algorithms first need to be assessed before it can be applied to point clouds which consists of flat areas and areas under a slope.

5.5 Limit of detection

The small area has a mean LoD of 5 mm, showing that the max values of 0.153 are mostly outliers. The spatial distribution of the LoD shows especially high values along the edges of the rocks. These extremes are most likely caused by the error in alignment. Just a minor shift in point clouds will result in a high standard deviation for areas with a steep gradient. The no data cells are clustered around the edges of some rocks. Apparently, even for a small area captured with a high photo density it is hard to capture all the details. This finding has implications for the applicability of the use of photo density to reach a certain level of precision (Fig. 9). For areas with a high roughness it is very likely that a much higher photo density should be used with a lot of different orientations to reach these precisions. Conversely Mancini et al. (2013) advised at least 10 overlapping images for areas with little surface texture, as such areas does not contain a lot of distinctive features. This shows that each area has their own characteristics and it is hard to come up with a generic photo density for a certain precision.

The LoD distribution of the large area shows large variation. At both sides an area with low LoD values is found. This implies that the pre and post erosion DSMs are closer to each other at these areas than in the middle or edges of the study area. Otherwise there would be no smaller standard deviation. The large area with longitudinal deformation has a mean LoD of 1.7 cm, when removing the trend the mean LoD decreased to 8.3 mm. This LoD is higher than the LoD of the small area. This was expected as the photo density decreased from 15 to 5 photos m^{-2}, but shows that the LoD is not lineair correlated with photo density.

The LoDs found are in the same order found in literature. Balaguer-Puig et al. (2017) found a spatial uniform 68% confidence LoD of 1 mm for a laboratory flume of 0.5 m^2. The lower LoD was reached as the data acquisition was in a controlled environment and the area of interest had a low roughness. Hänsel et al. (2016) found a spatial uniform 85% confidence LoD of 3.5 mm for 3 m^2 with a low roughness, which is comparable to the LoD of the small area. Eltner et al. (2015) found a spatial homogeneous LoD with a confidence interval of 90% of 1 cm for the use of SfM on a UAV on a plot size of 600 m^2. This LoD is 0.2 cm larger than the LoD for the trend adjusted area of 120 m^2 in this study.

Morgan et al. (2017) observed a non-linear longitudinal deformation in the SfM models of a 9 m long flume in a laboratory. The trend in differences between the DSMs along the x-axis found (Fig. 15a) can be explained by this non-linear longitudinal deformation. This so called doming effect in the DSMs could be caused by inaccuracies in the radial distortion models determined by PhotoScan for each photo.

Every camera adds its own special signature to a photo, PhotoScan corrects for this using camera parameters. The radial distortion of a lens, part of the signature of a camera, has a significant influence on the quality of a point cloud. Distortion increases with increasing distance from the centre of convergence (Peter Heng et al., 2010) and is highly correlated to the lens focal length (Mosbrucker et al., 2017). The small focal length used in this research should be increased to minimize radial distortion. However, the radial distortion still remains the most important parameter to be corrected for (Luhmann et al., 2013). Camera calibration prior to the capturing of the surface and fixate the obtained corrections in PhotoScan will decrease the doming effect.

Another factor of importance was found by Dietrich (2016), who concluded that having too much photos taken parallel instead of convergent can cause this doming effect (Fig 19). This is therefore frequently observed by the use of SfM with UAV data (James and Robson, 2014). This could cause the dome effect in this study as well, as the large study area was a vertical outcrop. The used systematic procedure to capture the whole study area in photos is easiest carried out to step 0.5 m side ways after a photo. This makes it prone for having too less convergent photos.

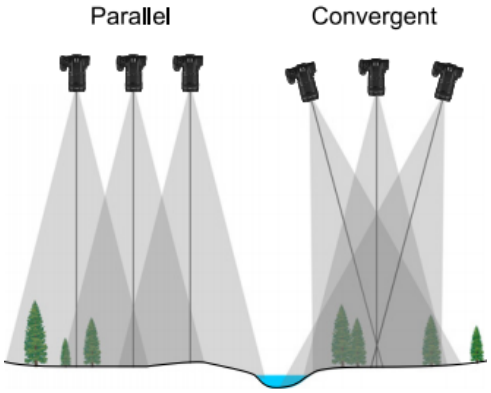

Figure 19: Illustration of parallel versus convergent camera orientations. Reprinted after Dietrich (2016).

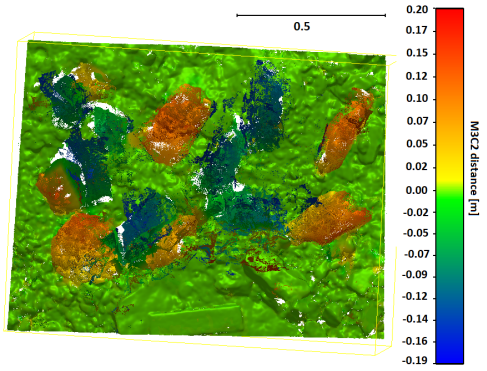

Figure 20: M3C2 algorithm applied on the small area. Mean distance of -6.6 mm, which includes the deviations caused by the relocation of rocks.

The doming effect is normally found when the SfM point cloud is compared to a reference lidar point cloud. In this study the doming effect is found by comparing two mean DSMs both created with SfM. For this reason can be concluded that the doming effect is not constant for the point clouds. This is partly caused by different camera locations and orientations of the photos. Another factor of influence could be the changing weather conditions.

Gienko and Terry (2014) found big differences in number of tie points when objects of interest were in directed sunlight and had some reflecting surfaces. This could explain the lower number of tie points found for the point clouds made of the post erosion situation as the sun broke through during photo acquisition of set 4. This difference in number of tie points influences the quality of image alignment and number of points in the final point cloud. This could explain the difference of degree in the doming effect along point clouds.

The trend removed in the DSMs resulted in a lower LoD. Removing a trend will remove some details and makes the reliability of the LoD unclear. Especially at the rows where large changes occurred. Pre erosion DSM 1 was the reference DSM where all the other 5 DSMs were corrected to. This results in a loss of detail in changes with post erosion DSMs. This can be observed as more false changes are observed along these rows compared to the detected changes with the doming effect (Fig. 17). Therefore the doming effect could best be minimized using fixed camera correction parameters in PhotoScan together with convergent photos. Removing the doming afterwards as done in this study is not preferable as detail is lost.

The use of cell by cell LoD can only be achieved by having the standard deviation for each cell. Using GCPs based on GPS coordinates to asses the precision of the DSM and calculate a LoD will result in uniform LoD for the area. This research showed that LoD is not spatially uniform. A uniform LoD will result in less precise determination of surface changes and will likely cause area specific over or under estimation of surface changes.

5.6 Volume calculation

The experiment with relocating stones showed a volume difference of 3.0 dm^3. A deviation of this order can be expected as it is on average 1.5 mm for the area of 2 m^2. In Section 4.3 mean deviations of 0.8 mm were found. Together with the possible addition of air spaces during the relocation of rocks could this explains the difference. According to Lague et al. (2013) the total error budget on change detection is dominated by the point clouds registration error and the surface roughness. This shows that the quality of a point cloud not only depends on the number of photos but also roughness of the surface should be considered. The use of a raster for volume calculations has the drawback of using 2D information instead of 3D data. Overhanging parts are impossible to capture using raster data.

A closed mesh is needed to calculate the volume including overhanging parts. Frankl et al. (2015) used SfM to understand gully dynamics in more detail. Using the OPTOCAT software they were able to close the created mesh and calculate volume differences. Kaiser et al. (2014) reconstructed the volume by calculating for every mesh a three-dimensional box to a predefined value in space.

When an area is conservative in sediment and the volume remains the same then the volume can be used as an validation number. This could be valuable as overhanging parts have a higher probability of creating shadow rich areas, which is known to decrease the quality of a point cloud built with SfM. When the exact changes in elevation or volume is not important, other methods to show erosion and deposition areas could be used. Lague et al. (2013) introduced the M3C2 algorithm which is capable of comparing aligned point clouds directly. The algorithm computes the distance between points along the normal surface direction and is therefore able to handle rough surfaces.

The M3C2 algorithm is included in CloudCompare and requires only a few parameters. Less pre processing is needed and therefore it is easy and fast in use. The changes in the small study area are well detected by the algorithm (Fig. 20). The mean C2C distance is 0.8 mm and 0.4 mm for the M3C2 distance of two point clouds of the unchanged situation. This in in agreement with findings by Smith and Vericat (2015), using point distances to asses quality shows lower errors than raster differencing. For future work it is advised to apply M3C2, as it easy, fast and shows areas of surface changes. Moreover, the more recent M3C2-PM is capable to include precision per point to detect surface changes (James et al., 2017). This new algorithm requires more steps and could therefore not be tested in this thesis. However, it could be a promising algorithm that includes a form of LoD and is able to handle rough surfaces.

5.7 Smart phone

The absolute mean difference between the DSLR DSMs and smart phone DSM is 3.0 cm. This shows that a smart phone creates a less similar DSM than DLSR DSMs between each other despite the fact that 900 photos were used compared to 600 photos of the DSLR. The median of 7.7 mm together with the observation of positive as negative difference indicates that there is no large bias in differences. The larger deviation than the DSLR DSMs could expected beforehand as the reprojection error given by PhotoScan was much higher for the smart phone photos.

Micheletti et al. (2015a) used 13 photos of a smart phone and 13 photos of a DSLR to build a point cloud of a 12 m^2 area and reached a median distance error of point to point of 5.3 mm and 3.8 mm compared to TLS reference data. This difference between the smart phone and DLSR is smaller compared to results found in this study. The comparison between point to point and raster differencing errors could explain this. Point to point quality quality assessment is less affected by the difference in point density between DSLR and a smart phone point cloud. For geomorphological analysis errors should be given when point clouds are processed to rasters or meshes to get an appropriate indication of the error.

Prosdocimi et al. (2017) found that errors in georeferencing calculated by the Agisoft Photoscan software are comparable for DSLR and smart phone for small plots of 0.25 m^2. The scaling errors in this study show similar results. This raises the question of the reliability of these errors generated by PhotoScan, as there is a larger difference between DSMs created with smart phones compared to DSLR.

5.8 Limitations & recommendations

Detecting surface changes at outcrops using SfM is already at a level that it can be put into practice as shown in this study. An important factor is the temporal frequency of your data acquisition. Old techniques to measure erosion colours certain areas and follow the colour to know the source area of the sediment. Identification of specific source areas is difficult with SfM, as in between the photo acquisition a source area could be filled up with sediment from above.

PhotoScan has been used as a tool to produce point clouds for further analysis. Settings advised in literature have been used, without an in depth sensitivity analysis. It is likely that the use of other settings in PhotoScan could improve the quality of the point cloud. The same holds for camera settings used in this research. Above all the author believes that these changes in settings will result in minor improvements compared to the quality increase that could be obtained by using more photos.

This research considered errors as a function of the number of photos m^{-2}. This generic approach could suggest that for each study area these numbers will be equal. However, the quality of SfM also dependent on the weather conditions, camera-object distance and the number of unique features, colours, texture and roughness of a study area. Therefore, these numbers should be used as a guideline, but showed that an increasing photo density results in smaller differences between the generated DSMs.

The choice of a cell size of 2.5 mm allows surface change detection at a small scale. This research showed that for areas without a lot of variation in elevation, differences between 2.5 mm cells are low. However, it can be hypothesized that for rough areas with a lot of steep gradients a larger cell size should be used considering the uncertainty in SfM models and alignment procedure seen in this research. The uncertainty in the 2D locations becomes too large, which will result in differences not caused by surface changes but by comparing different locations of the study area.

The uncertainty in change detection can be assessed by the use of 3 DSMs of an unchanged area without the need of GPS system. This methodology allows for LoD calculation on a cell specific level. The use of GPS measured GCPs in combination of only 1 DSM of the pre and post situation will result in an area uniform LoD. However, the use of GPS has the big advantage that alignment of different point clouds in time can be done automatically. The presented method in this research requires static alignment point in space and time to detect surface changes. Screws drilled in the study area or solid natural features present could be used for this alignment.

The applied formula to calculate the LoD takes into account differences in height values caused by PhotoScan and the alignment. However, only the alignment deviation between the 3 DSMs in a set is taken into account. The alignment error between the pre- and post DSMs is not taken into account. Consequently the LoD is likely a little higher than presented in this research.

Longitudinal deformation affected the similarity of point clouds. It is advised to use a larger fixed focal length than f/14 used in this study. Radial distortion is most visible at a small focal length. In addition the camera should be calibrated to obtain fixed correction parameters that can be used in PhotoScan. Different methods of calibration are evaluated in Balletti et al. (2014) and could be used as a guideline for further work. Implementation of these two advices together with enough convergent photos should result in point clouds with no doming effect.

During the research ideas popped up to include the factor number of points in a cell to calculate the LoD. This would not work for the reason that SfM does not produce a homogeneous point distribution as TLS does. Unique features with a lot of texture will have a higher point density to a flat areas without any colour differences. This does not mean that the uncertainty for the flat area should be lower than for unique features. Lidar systems, such as a TLS with a homogeneous scanning pattern would be suitable to include the factor point density per cell.

6 Conclusions

This study was conducted to enhance the understanding of uncertainty when using SfM or a hand-held lidar system to monitor surface changes at rock outcrops. Several studies conducted comparable experiments, but were mostly in a controlled environment. Both techniques can be used without the need of GPS control points, which makes them cheap and easy to carry to remote mountainous area. Three aspects of these techniques were investigated. First, the effect and importance of sampling strategy was assessed. Next, the variation within DSMs when created with an equal sampling strategy was determined. These two steps came together by determining the ability to detect surface changes using a cell specific Limit of Detection (LoD).

The hand held lidar system ZEB1 produced point clouds of an insufficient density with a lot of noise. In addition the manual alignment of the uncoloured point clouds of the ZEB1 introduced variation in DSMs of several dm. For these reasons the hand-held lidar system was not capable to detect surface changes at a small scale and the uncertainty could not be determined.

SfM was able to generate similar point clouds of unchanged areas at outcrops. The differences among rasters created from point clouds decreases with the number of photos per area. A low photo density can affect the photo alignment in PhotoScan and as a consequence the coverage of an area. However, even the low photo density of 3 photos m^{-2} was able to capture the major height patterns. It is important to create a raster along the normal direction of an outcrop. The processing time increases with the number of photos, but in general it is advised to take as much photos given the total available time for the best quality. Quality parameters given by PhotoScan should only be used as a first indication.

90% of the differences between 6 unique DSMs of an unchanged area created with a photo density of 8 photos m^{-2} are within -3 and 3 mm. This proves that SfM is capable of repeatable generating consistent point clouds of unchanged areas in outdoor conditions. Differences are caused by the input of unique sets of photos and manual alignment of point clouds.

To include the uncertainty in monitoring surface changes 3 unique DSMs were made at each time step. After human induced erosion again 3 DSMs were made. The standard deviation of these 2 sets of 3 DSMs was used to calculate the LoD. Only surface changes larger than the LoD can reliably be detected.

A case study of 2 m^2 had a mean LoD of 5 mm. The LoD showed large spatial variation, especially at regions with steep gradients. This was caused by the deviations in alignment of point clouds. It showed that the use of cell specific LoD is more preferred than an area homogeneous LoD. When the area was increased to 120 m^2 the mean LoD increased to 1.7 cm. However, there were clustered regions at both sides of this outcrop with low LoD values. These spatial difference were caused by non-linear longitudinal deformation of the point clouds along the x-axis. This deformation was not equal for all point clouds, causing structural differences. Fixed camera corrections parameters, larger focal length and more convergent camera orientations could decrease this so called doming effect in future work.

An afterwards correction for this deformation resulted in a mean LoD of 8.3 mm. This correction not only removed the deformation but also some noise caused by the processing chain. Therefore, DSMs without the doming effect could have a higher more realistic LoD than presented in this study. Human induced surface changes were detected, together with regions of small false detected changes. The alignment deviation between pre- and post erosion set of DSMs were not taken into account by calculating the LoD and is likely the cause of these false positives.

This study shows that SfM is able to produce consistent point clouds in outdoor conditions at the mm-scale. SfM is ready to be widely applied to monitor surface changes using a cell specific LoD. The hand-held lidar scanner produced point clouds of insufficient quality. Future work could be done on increasing the precision of the alignment among sets of DSMs, determine optimal cell sizes and evaluate the suggested sampling strategy to prevent longitudinal deformation of large point clouds.

References

Adobe Systems Software Ireland Ltd., 2018. Adobe Digital Negative Converter.
URL https://helpx.adobe.com/nl/photoshop/using/adobe-dng-converter.html

Agisoft, 2014. Agisoft Photoscan. Professional Edition.

Aguilar, F. J., Mills, J., et al., 2008. Accuracy assessment of LiDAR-derived digital elevation models. The Photogrammetric Record 23 (122), 148–169.

Bailey, T., Durrant-Whyte, H., 2006. Simultaneous localization and mapping (SLAM): Part ii. IEEE Robotics & Automation Magazine 13 (3), 108–117.

Balaguer-Puig, M., Marqués-Mateu, Á., Lerma, J. L., Ibáñez-Asensio, S., 2017. Estimation of small-scale soil erosion in laboratory experiments with Structure from Motion photogrammetry. Geomorphology.

Balletti, C., Guerra, F., Tsioukas, V., Vernier, P., 2014. Calibration of action cameras for photogrammetric purposes. Sensors 14 (9), 17471–17490.

Bauwens, S., Bartholomeus, H., Calders, K., Lejeune, P., 2016. Forest inventory with terrestrial LiDAR: A comparison of static and hand-held mobile laser scanning. Forests 7 (6), 127.

Bechet, J., Duc, J., Jaboyedoff, M., Loye, A., Mathys, N., 2015. Erosion processes in black marl soils at the millimetre scale: preliminary insights from an analogous model. Hydrology and Earth System Sciences 19 (4), 1849–1855.

Beer, A. R., Kirchner, J. W., Turowski, J. M., 2016. Graffiti for science-erosion painting reveals spatially variable erosivity of sediment-laden flows. Earth Surface Dynamics 4 (4), 885.

Bierman, P. R., Caffee, M., 2001. Slow rates of rock surface erosion and sediment production across the Namib desert and escarpment, southern Africa. American Journal of Science 301 (4-5), 326–358.

Bistacchi, A., Balsamo, F., Storti, F., Mozafari, M., Swennen, R., Solum, J., Tueckmantel, C., Taberner, C., 2015. Photogrammetric digital outcrop reconstruction, visualization with textured surfaces, and three-dimensional structural analysis and modeling: Innovative methodologies applied to fault-related dolomitization (Vajont limestone, Southern Alps, Italy). Geosphere 11 (6), 2031–2048.

Bosse, M., Zlot, R., Flick, P., 2012. Zebedee: Design of a spring-mounted 3D range sensor with application to mobile mapping. IEEE Transactions on Robotics 28 (5), 1104–1119.

Brasington, J., Langham, J., Rumsby, B., 2003. Methodological sensitivity of morphometric estimates of coarse fluvial sediment transport. Geomorphology 53 (3-4), 299–316.

Cao, M., Li, S., Jia, W., Li, S., Liu, X., 2017. Robust bundle adjustment for large-scale Structure from Motion. Multimedia Tools and Applications 76 (21), 21843–21867.

Carrivick, J. L., Smith, M. W., Quincey, D. J., 2016. Structure from Motion in the Geosciences. John Wiley & Sons.

Chen, Z., Gao, B., Devereux, B., 2017. State-of-the-art: DTM generation using airborne lidar data. Sensors 17 (1), 150.

Chidburee, P., Mills, J., Miller, P., Fieber, K., 2016. Towards a low-cost, real-time photogrammetric landslide monitoring system utilising mobile and cloud computing technology. International Archives of the Photogrammetry, Remote Sensing & Spatial Information Sciences 41.

Collins, S. L., Knapp, A. K., Briggs, J. M., Hartnett, D. C., 1998. Grassland Dynamics: Long-term ecological research in talgrass prairie. Science.

De Vente, J., Poesen, J., Verstraeten, G., Govers, G., Vanmaercke, M., Van Rompaey, A., Arabkhedri, M., Boix-Fayos, C., 2013. Predicting soil erosion and sediment yield at regional scales: Where do we stand? Earth-Science Reviews 127, 16–29.

Dewez, T. J., Plat, E., Degas, M., Richard, T., Pannet, P., Thuon, Y., Meire, B., Watelet, J.-M., Cauvin, L., Lucas, J., et al., 2016. Handheld Mobile Laser Scanners ZEB-1 and ZEB-Revo to map an underground quarry and its above-ground surroundings. In: 2nd Virtual Geosciences Conference: VGC 2016.

Dietrich, J. T., 2016. Riverscape mapping with helicopter-based Structure-from-Motion photogrammetry. Geomorphology 252, 144–157.

Dixon, B., Earls, J., 2009. Resample or not?! Effects of resolution of DEMs in watershed modeling. Hydrological Processes 23 (12), 1714–1724.

Durrant-Whyte, H., Bailey, T., 2006. Simultaneous Localisation and Mapping (SLAM): part i the essential algorithms.

Eltner, A., Baumgart, P., 2015. Accuracy constraints of terrestrial LiDAR data for soil erosion measurement: Application to a Mediterranean field plot. Geomorphology 245, 243–254.

Eltner, A., Baumgart, P., Maas, H.-G., Faust, D., 2015. Multi-temporal UAV data for automatic measurement of rill and interrill erosion on loess soil. Earth Surface Processes and Landforms 40 (6), 741–755.

Eltner, A., Kaiser, A., Castillo, C., Rock, G., Neugirg, F., Abellán, A., 2016. Image-based surface reconstruction in geomorphometry–merits, limits and developments. Earth Surface Dynamics 4 (2), 359–389.

Fischler, M. A., Bolles, R. C., 1987. Random sample consensus: a paradigm for model fitting with applications to image analysis and automated cartography. In: Readings in computer vision. Elsevier, pp. 726–740.

Fonstad, M. A., Dietrich, J. T., Courville, B. C., Jensen, J. L., Carbonneau, P. E., 2013. Topographic Structure from Motion: a new development in photogrammetric measurement. Earth Surface Processes and Landforms 38 (4), 421–430.

Frankl, A., Stal, C., Abraha, A., Nyssen, J., Rieke-Zapp, D., De Wulf, A., Poesen, J., 2015. Detailed recording of gully morphology in 3D through image-based modelling. Catena 127, 92–101.

Geyh, M. A., Schleicher, H., 2012. Absolute age determination: physical and chemical dating methods and their application. Springer Science & Business Media.

Gienko, G. A., Terry, J. P., 2014. Three-dimensional modeling of coastal boulders using multi-view image measurements. Earth surface processes and Landforms 39 (7), 853–864.

Gindraux, S., Boesch, R., Farinotti, D., 2017. Accuracy assessment of digital surface models from unmanned aerial vehicles imagery on glaciers. Remote Sensing 9 (2), 186.

Girardeau-Montaut, D., R&D, E., ParisTech, T., 2018. CloudCompare.
URL `http://www.cloudcompare.org/`

Gulam, V., Gajski, D., Podolszki, L., 2018. Photogrammetric measurement methods of the gully rock wall retreat in Istrian badlands. CATENA 160, 298–309.

Guth, P. L., 2006. Geomorphometry from srtm. Photogrammetric Engineering & Remote Sensing 72 (3), 269–277.

Hänsel, P., Schindewolf, M., Eltner, A., Kaiser, A., Schmidt, J., 2016. Feasibility of high-resolution soil erosion measurements by means of rainfall simulations and SfM photogrammetry. Hydrology 3 (4), 38.

Heritage, G., Large, A., 2009. Laser scanning for the environmental sciences. John Wiley & Sons.

Hladik, C., Alber, M., 2012. Accuracy assessment and correction of a LiDAR-derived salt marsh digital elevation model. Remote Sensing of Environment 121, 224–235.

Hodge, R. A., 2010. Using simulated terrestrial laser scanning to analyse errors in high-resolution scan data of irregular surfaces. ISPRS Journal of Photogrammetry and Remote Sensing 65 (2), 227–240.

James, M. R., Quinton, J. N., 2014. Ultra-rapid topographic surveying for complex environments: the hand-held mobile laser scanner (HMLS). Earth surface processes and landforms 39 (1), 138–142.

James, M. R., Robson, S., 2014. Mitigating systematic error in topographic models derived from UAV and ground-based image networks. Earth Surface Processes and Landforms 39 (10), 1413–1420.

James, M. R., Robson, S., Smith, M. W., 2017. 3-d uncertainty-based topographic change detection with Structure-from-Motion photogrammetry: precision maps for ground control and directly georeferenced surveys. Earth Surface Processes and Landforms 42 (12), 1769–1788.

Kaiser, A., Neugirg, F., Rock, G., Müller, C., Haas, F., Ries, J., Schmidt, J., 2014. Small-scale surface reconstruction and volume calculation of soil erosion in complex Moroccan gully morphology using Structure from Motion. Remote Sensing 6 (8), 7050–7080.

Krabill, W., Collins, J., Link, L., Swift, R., Butler, M., 1984. Airborne laser topographic mapping results. Photogrammetric Engineering and remote sensing 50 (6), 685–694.

Kundzewicz, Z. W., Mata, L. J., Arnell, N., Doll, P., Kabat, P., Jimenez, B., Miller, K., Oki, T., Zekai, S., Shiklomanov, I., 2007. Freshwater resources and their management.

Lague, D., Brodu, N., Leroux, J., 2013. Accurate 3D comparison of complex topography with terrestrial laser scanner: Application to the Rangitikei canyon (NZ). ISPRS journal of photogrammetry and remote sensing 82, 10–26.

Lamb, M. P., Fonstad, M. A., 2010. Rapid formation of a modern bedrock canyon by a single flood event. Nature Geoscience 3 (7), 477.

Lowe, D. G., 1999. Object recognition from local scale-invariant features. In: Computer vision, 1999. The proceedings of the seventh IEEE international conference on. Vol. 2. Ieee, pp. 1150–1157.

Lu, X., Li, Y., Washington-Allen, R. A., Li, Y., Li, H., Hu, Q., 2017. The effect of grid size on the quantification of erosion, deposition, and rill network. International Soil and Water Conservation Research 5 (3), 241–251.

Luhmann, T., Robson, S., Kyle, S., Boehm, J., 2013. Close-range photogrammetry and 3D imaging. Walter de Gruyter.

Makadia, A., Patterson, A., Daniilidis, K., 2006. Fully automatic registration of 3D point clouds. In: Computer Vision and Pattern Recognition, 2006 IEEE Computer Society Conference on. Vol. 1. IEEE, pp. 1297–1304.

Mancini, F., Dubbini, M., Gattelli, M., Stecchi, F., Fabbri, S., Gabbianelli, G., 2013. Using unmanned aerial vehicles (UAV) for high-resolution reconstruction of topography: The Structure from Motion approach on coastal environments. Remote Sensing 5 (12), 6880–6898.

Micheletti, N., Chandler, J. H., Lane, S. N., 2015a. Investigating the geomorphological potential of freely available and accessible Structure-from-Motion photogrammetry using a smartphone. Earth Surface Processes and Landforms 40 (4), 473–486.

Micheletti, N., Chandler, J. H., Lane, S. N., 2015b. Structure from motion (SfM) photogrammetry.

Miller, K. B., West, R. R., 1993. Reevaluation of wolfcampian cyclothems in northeastern Kansas: significance of subaerial exposure and flooding surfaces. Kansas Geological Survey Bulletin 235, 1–26.

Montgomery, D. R., Brandon, M. T., 2002. Topographic controls on erosion rates in tectonically active mountain ranges. Earth and Planetary Science Letters 201 (3-4), 481–489.

Morgan, J. A., Brogan, D. J., Nelson, P. A., 2017. Application of Structure-from-Motion photogrammetry in laboratory flumes. Geomorphology 276, 125–143.

Mosbrucker, A. R., Major, J. J., Spicer, K. R., Pitlick, J., 2017. Camera system considerations for geomorphic applications of SfM photogrammetry. Earth Surface Processes and Landforms 42 (6), 969–986.

Mukherjee, S., Joshi, P., Mukherjee, S., Ghosh, A., Garg, R., Mukhopadhyay, A., 2013. Evaluation of vertical accuracy of open source digital elevation model (DEM). International Journal of Applied Earth Observation and Geoinformation 21, 205–217.

Muratov, O., Slynko, Y., Chernov, V., Lyubimtseva, M., Shamsuarov, A., Bucha, V., 2016. 3DCapture: 3D reconstruction for a smartphone. In: Proceedings of the IEEE Conference on Computer Vision and Pattern Recognition Workshops. pp. 75–82.

Nocerino, E., Menna, F., Remondino, F., Toschi, I., Rodríguez-Gonzálvez, P., 2017. Investigation of indoor and outdoor performance of two portable mobile mapping systems. In: Videometrics, Range Imaging, and Applications XIV. Vol. 10332. International Society for Optics and Photonics, p. 103320I.

Pachauri, R. K., Allen, M. R., Barros, V. R., Broome, J., Cramer, W., Christ, R., Church, J. A., Clarke, L., Dahe, Q., Dasgupta, P., et al., 2014. Climate change 2014: synthesis report. Contribution of Working Groups I, II and III to the fifth assessment report of the Intergovernmental Panel on Climate Change. IPCC.

Patel, A., 2012. Mountain erosion and mitigation: global state of art. Environmental Earth Sciences 66 (6), 1631–1639.

Peter Heng, B., Chandler, J. H., Armstrong, A., 2010. Applying close range digital photogrammetry in soil erosion studies. The Photogrammetric Record 25 (131), 240–265.

Piermattei, L., Carturan, L., Guarnieri, A., 2015. Use of terrestrial photogrammetry based on structure-from-motion for mass balance estimation of a small glacier in the Italian alps. Earth Surface Processes and Landforms 40 (13), 1791–1802.

Pimentel, D., Harvey, C., Resosudarmo, P., Sinclair, K., Kurz, D., McNair, M., Crist, S., Shpritz, L., Fitton, L., Saffouri, R., et al., 1995. Environmental and economic costs of soil erosion and conservation benefits. Science-AAAS-Weekly Paper Edition 267 (5201), 1117–1122.

Piras, M., Taddia, G., Forno, M. G., Gattiglio, M., Aicardi, I., Dabove, P., Russo, S. L., Lingua, A., 2017. Detailed geological mapping in mountain areas using an unmanned aerial vehicle: application to the Rodoretto Valley, NW Italian Alps. Geomatics, Natural Hazards and Risk 8 (1), 137–149.

Prosdocimi, M., Burguet, M., Di Prima, S., Sofia, G., Terol, E., Comino, J. R., Cerdà, A., Tarolli, P., 2017. Rainfall simulation and Structure-from-Motion photogrammetry for the analysis of soil water erosion in Mediterranean vineyards. Science of the Total Environment 574, 204–215.

Reutebuch, S. E., McGaughey, R. J., Andersen, H.-E., Carson, W. W., 2003. Accuracy of a high-resolution lidar terrain model under a conifer forest canopy. Canadian journal of remote sensing 29 (5), 527–535.

Riquelme, A., Cano, M., Tomás, R., Abellán, A., 2017. Identification of rock slope discontinuity sets from laser scanner and photogrammetric point clouds: A comparative analysis. Procedia engineering 191, 838–845.

RStudio, 2018. Rstudio: integrated development for R. RStudio, Inc., Boston, MA URL http://www. rstudio. com.

Rusu, R. B., Blodow, N., Marton, Z. C., Beetz, M., 2008. Aligning point cloud views using persistent feature histograms. In: Intelligent Robots and Systems, 2008. IROS 2008. IEEE/RSJ International Conference on. IEEE, pp. 3384–3391.

Ryding, J., Williams, E., Smith, M. J., Eichhorn, M. P., 2015. Assessing handheld mobile laser scanners for forest surveys. remote sensing 7 (1), 1095–1111.

Sanz-Ablanedo, E., Chandler, J. H., Wackrow, R., 2012. Parameterising internal camera geometry with focusing distance. The Photogrammetric Record 27 (138), 210–226.

Saputra, A., Gomez, C., Delikostidis, I., Zawar-Reza, P., Hadmoko, D. S., Sartohadi, J., Setiawan, M. A., 2018. Determining earthquake susceptible areas Southeast of Yogyakarta, Indonesia outcrop analysis from Structure from Motion (sfm) and Geographic Information System (gis). Geosciences 8 (4), 132.

Schonberger, J. L., Frahm, J.-M., 2016. Structure-from-Motion revisited. In: Proceedings of the IEEE Conference on Computer Vision and Pattern Recognition. pp. 4104–4113.

Sirmacek, B., Shen, Y., Lindenbergh, R., Diakite, A., Zlatanova, S., 2016. Comparison of ZEB1 and leica c10 indoor laser scanning point clouds. ISPRS Annals of the Photogrammetry, Remote Sensing and Spatial Information Sciences 3.

Smith, M. W., Vericat, D., 2015. From experimental plots to experimental landscapes: topography, erosion and deposition in sub-humid badlands from Structure-from-Motion photogrammetry. Earth Surface Processes and Landforms 40 (12), 1656–1671.

Tam, G. K., Cheng, Z.-Q., Lai, Y.-K., Langbein, F. C., Liu, Y., Marshall, D., Martin, R. R., Sun, X.-F., Rosin, P. L., 2013. Registration of 3D point clouds and meshes: a survey from rigid to nonrigid. IEEE transactions on visualization and computer graphics 19 (7), 1199–1217.

Triggs, B., McLauchlan, P. F., Hartley, R. I., Fitzgibbon, A. W., 1999. Bundle adjustment: a modern synthesis. In: International workshop on vision algorithms. Springer, pp. 298–372.

Turowski, J. M., Badoux, A., Leuzinger, J., Hegglin, R., 2013. Large floods, alluvial overprint, and bedrock erosion. Earth Surface Processes and Landforms 38 (9), 947–958.

Turowski, J. M., Cook, K. L., 2017. Field techniques for measuring bedrock erosion and denudation. Earth Surface Processes and Landforms 42 (1), 109–127.

Vanwalleghem, T., Laguna, A., Giráldez, J., Jiménez-Hornero, F., 2010. Applying a simple methodology to assess historical soil erosion in olive orchards. Geomorphology 114 (3), 294–302.

Verhoeven, G., Doneus, M., Briese, C., Vermeulen, F., 2012. Mapping by matching: a computer vision-based approach to fast and accurate georeferencing of archaeological aerial photographs. Journal of Archaeological Science 39 (7), 2060–2070.

Vinci, A., Todisco, F., Brigante, R., Mannocchi, F., Radicioni, F., 2017. A smartphone camera for the structure from motion reconstruction for measuring soil surface variations and soil loss due to erosion. Hydrology Research 48 (3), 673–685.

Westoby, M., Brasington, J., Glasser, N., Hambrey, M., Reynolds, J., 2012. Structure-from-Motion photogrammetry: A low-cost, effective tool for geoscience applications. Geomorphology 179, 300–314.

Wheaton, J. M., 2008. Uncertainty in morphological sediment budgeting of rivers. Unpublished PhD, University of Southampton, Southampton 412.

Wheaton, J. M., Brasington, J., Darby, S. E., Sear, D. A., 2010. Accounting for uncertainty in DEMs from repeat topographic surveys: improved sediment budgets. Earth Surface Processes and Landforms 35 (2), 136–156.

Williams, R., 2012. Section 2.3. 3: DEMs of Difference. Geomorphological Techniques(Online Edition). British Society for Geomorphology: London, UK.

Wróżyński, R., Pyszny, K., Sojka, M., Przybyła, C., Murat-Błażejewska, S., 2017. Ground volume assessment using Structure from Motion photogrammetry with a smartphone and a compact camera. Open Geosciences 9 (1), 281–294.

Xiang, T., Cheong, L.-F., 2003. Understanding the behavior of SfM algorithms: A geometric approach. International Journal of Computer Vision 51 (2), 111–137.

Zhang, W., Montgomery, D. R., 1994. Digital elevation model grid size, landscape representation, and hydrologic simulations. Water resources research 30 (4), 1019–1028.

Appendices

A High vs medium density setting PhotoScan

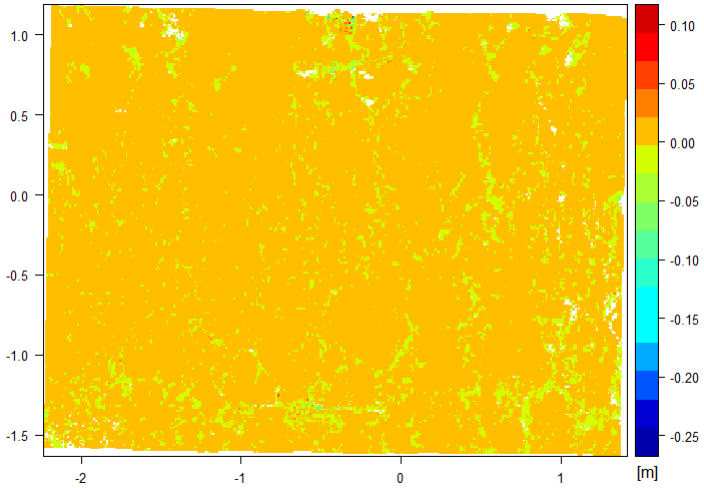

Figure A.1: Comparison of the influence of the setting Build Dense Pointcloud in Photoscan between high and medium. The difference has been calculated as raster high density pointcloud minus the medium dense pointcloud raster. The DSMs are based on 200 photos. The absolute mean error between the DSM is 1.6 mm. The mean of the difference population is -0.9 mm, with a standard deviation of 3.4 mm.

B Work flow description PhotoScan & CloudCompare

Print markers

"Tools > Markers > Print Markers"
Default settings can be used. Depending on the expected camera-object distances marker sizes could be increased or decreased.

Add photos
To add photo select "Add Photos..." command from Workflow menu

Photos are Shown in "Chunk 1". Chunks can be used as (1) projects on their own or (2) to split up large projects and align chunks after the processing. It this tutorial it is advised to use only 1 chunk, even for large photo sets as the quality of the output decreases when splitting a project up in chunks according to online experiences.

Detect Markers (only when markers were used)
"Tools > Markers > Detect Markers"

Align photos
"Workflow > Align Photos" (Fig. B.1)

Accuracy must be set to highest to use the full resolution of the photos. Medium will use 50% of the resolution and low 25% of the resolution.

Pair preselection: can be set when using high resolution photos. "Generic" setting will Photoscan make a quick pre-scan to see which photos share the same view. When photos do not share the same view a detail comparison per pixel makes no sense. This decreases the processing time a lot and has no impact on the quality when using DSLR photos.

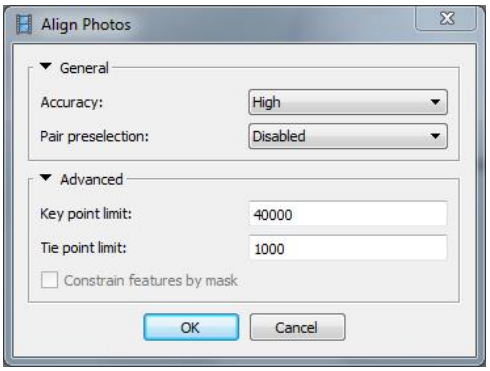

Figure B.1: Align photo screen in Agisoft PhotoScan.

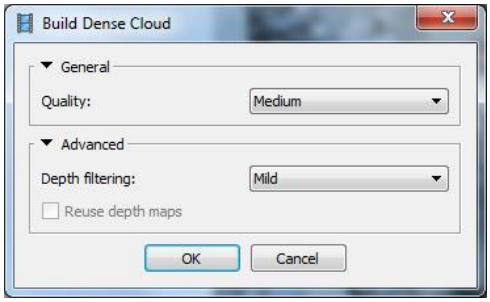

Figure B.2: Build dense point cloud screen in Agisoft PhotoScan.

Key point limit: the maximum number of points PhotoScan will extract from each photo. For a 36 Megapixel photo the maximum number of points than can be extracted is usually around 240000. Online experiences showed that an increase of the default value is not necessary. Using a higher value will result in more points in the Sparse point cloud. A value 0 will use the maximum number of points.

Tie point limit: determines the number of points that will be used for the alignment detected from the key points. For example when key point is 40000 and tie point set to 1000, only the 1000 best key points will be used. A value 0 will use the maximum number of points.

Gradual selection & optimize cameras
"Edit > Gradual selection > Reprojection Error > 0.5" (remove points with high error)

Reconstruction uncertainty: An example is when there are only two camera and a point is being triangulated by intersection of two rays there is a direction in which the variation for the point position is maximal and another direction with a minimal variations. Dividing one on another (max to min) results in the reconstruction uncertainty value. This criterion was designed for visualization and estimating the errors. It can be seen as a value that characterizes the accuracy of positioning points in clouds.

Reprojection error: characterizes the accuracy of point positioning and has the unit pixels. Before optimizing the camera point with a huge reprojection error should be removed. A value of 0.5 has been used in this research, but is case dependent.

"Tools > Optimize Camera" This study applied optimisation to all parameters expect for Skew and Fit aspect as these are 0 in normal frame cameras.

F: focal length measured in pixels
Cx, cy: principal point coordinates, coordinates of lens optical axis interception with sensor plane.
Skew: skew transformation coefficient.
k: radial distortion coefficients.
p: tangential distortion coefficients.

Build dense point cloud
"Work flow > Build Dense Cloud" (Fig. B.2)

Quality: Medium (used in this research). Photos are down sampled by a factor 4 compared to high.
Depth filtering:
Mild (used in this research). Recommend when scene to be reconstructed is complex with small details
Aggressive: sort out most of the outliers, scene does not contain meaningful small details.
Moderate: between mild and aggressive, Agisoft advise to experiment with these settings.

Figure B.3: Create scale bar of two markers.

Scale point cloud
"Select two markers > Create Scale Bar" (Fig. B.3)
"Reference Tab (bottom left) > Input known distances scale bars > Update"

Estimated errors per scale bar are shown in the third column.

Export point cloud
"File > Export Points > Save as type: .las"

CloudCompare

Load point cloud and put horizontal
"File > Open > Select point cloud of choice"
"Tools > fit > plane"

"Property of the point cloud > Align camera (Fig. B.4) > CTRL C transformation matrix in console (bottom)"
"Edit > Apply transformation > CNTRL V matrix > Apply"

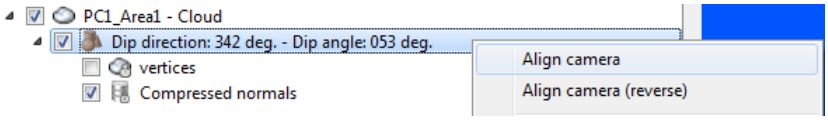

Figure B.4: Align camera on created plane.

Alignment

"Align two point clouds by at least picking three point (Fig. B.5) > Select consistent reference for point clouds > Pick at least three points > Align > Write down RMSE reached"

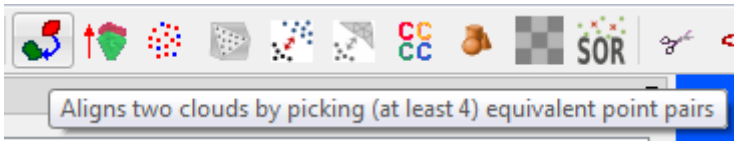

Figure B.5: Align camera on created plane.

Crop study area
"Select all aligned point clouds in tree > Segment tool > Select Study area"
Rasterize
"Select point cloud > rasterize > put in parameters"

C Effect cell size on number of empty cells

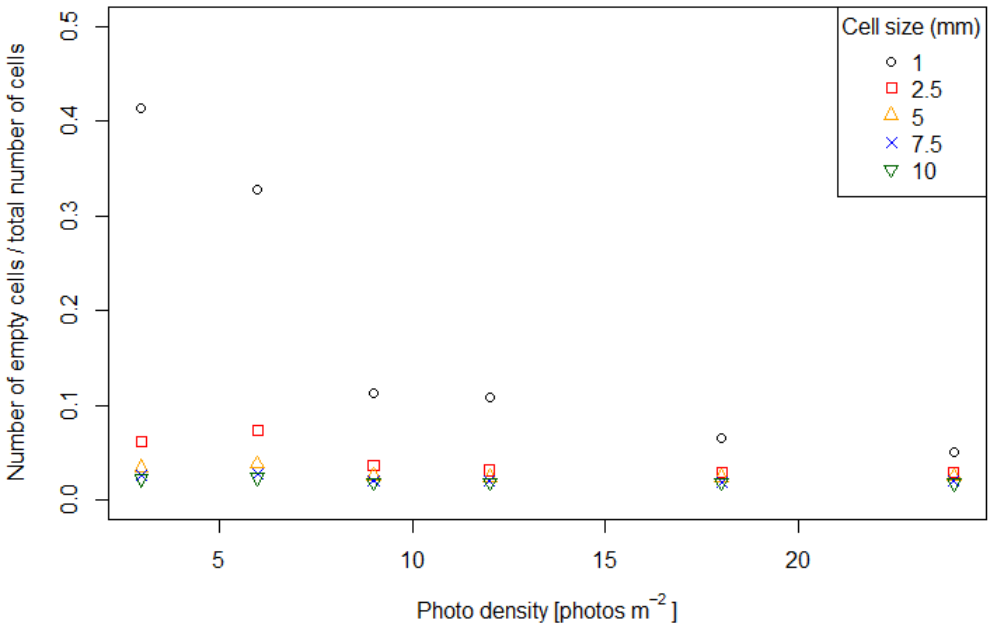

Figure C.1: Effect of cell size on the number of empty cells in a raster. The same point clouds have been used with different cell sizes. The y-axis shows the percentage of empty cells of total number of cells.

D Errors scale bars

Table D.1: Errors with the scale bars generated with PhotoScan for the 6 point clouds each generated with 100 pictures.

Errors (cm)	pc 1	pc 2	pc 3	pc 4	pc 5	pc 6
target 26 - 28	-0,478	0,094	0,106	0,119	0,093	0,090
target 26 - 29	0,376	0,125	0,110	0,083	0,134	0,124
target 13 - 18	0,006	0,133	0,135	0,115	0,138	0,145
target 13 - 15	-0,479	0,017	0,022	0,042	-0,467	-0,473
target 9 - 10	0,187	-0,463	-0,466	-0,449	0,010	0,007
target 7 - 8	0,073	-0,467	-0,476	-0,468	-0,476	-0,467
target 11 - 12	0,127	0,051	0,066	0,057	0,051	0,059
Average absolute error	0,247	0,193	0,197	0,191	0,195	0,195
Variables from Photoscan						
tiepoints	111.735	126.736	117.867	140.729	118.703	126.054
reprojection error (pix)	0,774	0,844	0,769	0,784	0,788	0,763
points	20.327.509	23.403.839	23.060.516	21.361.835	20.276.532	22.608.138
effective overlap	3,53337	3,02364	3,28458	2,98977	3,07823	2,90718

Table D.2: Errors with the scale bars generated with PhotoScan for the 6 point clouds each generated with 600 pictures. 3 point clouds (pc 1 to pc 3) before an erosion event and 3 after (pc 4 to pc 6). The point cloud generated with photos from a cellphone for the study area past erosion

Errors	pc 1	pc 2	pc 3	pc 4	pc 5	pc 6	Cellphone
target 7 - 8	-0,0123	-0,0895	-0,0047	0,0065	-0,0455	0,0035	-0,0761
target 9 -10	0,0081	-0,0177	0,0442	0,0055	-0,0258	-0,0607	-0,0298
target 43 - 44	0,0238	0,0439	-0,0420	0,0076	0,0883	0,0504	0,0266
target 15 - 16	0,0503	-0,0158	0,0321	-0,0128	0,0705	0,0169	0,0826
target 13 - 18	-0,0433	0,0981	-0,0144	-0,0085	-0,0413	-0,0042	0,0348
Average absolute error	0,0276	0,0530	0,0275	0,0082	0,0543	0,0272	0,0500
Variables from Photoscan							
tiepoints	766.560	598.332	590.558	561.587	549.820	544.212	416.686
reprojection error (pix)	0,678	0,771	0,801	0,721	0,762	0,812	4,7
points	132.287.808	98.862.093	87.259.070	87.732.812	83.460.099	89.116.942	44.239.778
effective overlap	3,54	4,65	5,35	4,95	5,20	5,37	6,63

E ZEB1 Point cloud

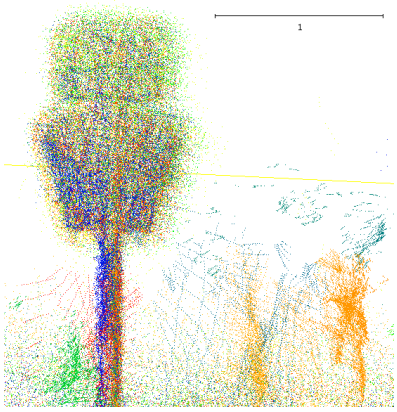

Figure E.1: Part of the point cloud, showing a traffic sign just next to the outcrop. The colour of the points represent the time of acquisition. The traffic sign shows no clear boundaries around the edges. Scale bar in [m].

F Change detection

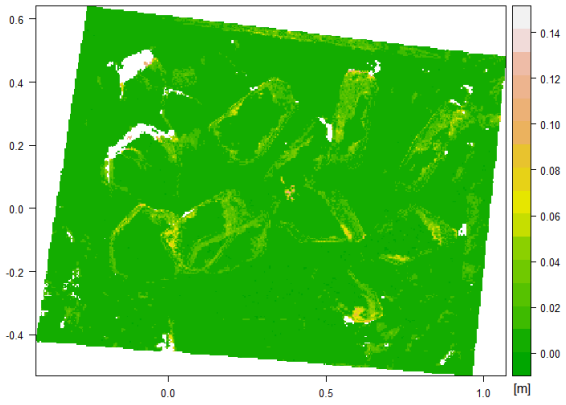

Figure F.1: The Limit of Detection of the small test area.

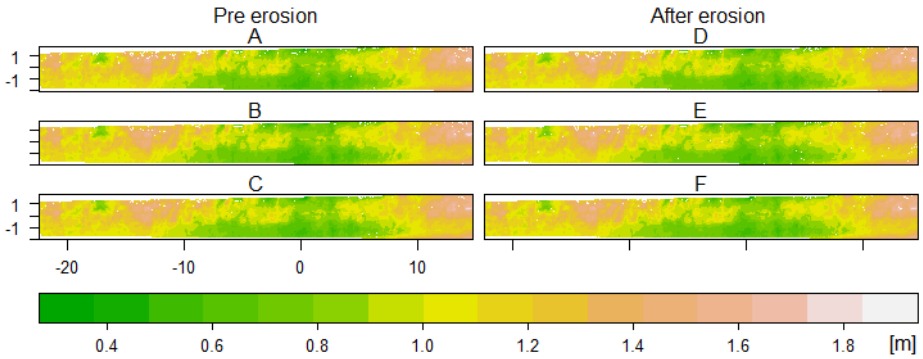

Figure F.2: Set of the 6 DSMs used for the LoD calculation. Left column are the pre erosion DSMs whereas the right column is after erosion DSMs

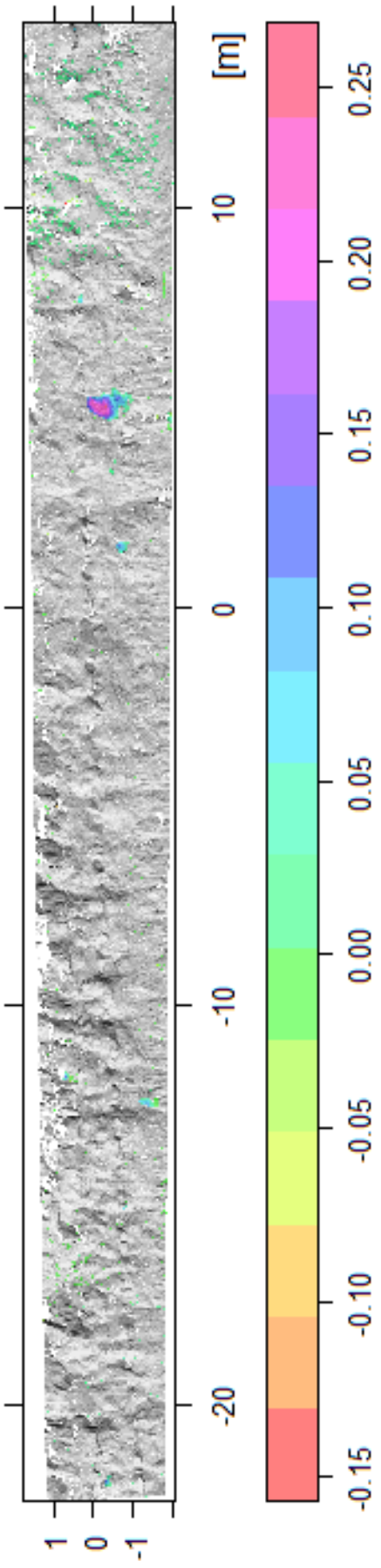

Figure F.3: Difference between the mean of the 3 DSMs before erosion and mean of 3 DSMs after erosion. Only changes larger that the LoD with the longitudual deformation have been plotted on the hillshade of the outcrop.